

Ultrarapid Optical Frequency-Domain Reflectometry Based Upon Dispersion-Induced Time Stretching: Principle and Applications

Tae-Jung Ahn, Yongwoo Park, and José Azaña, *Member, IEEE*

(Invited Paper)

Abstract—This paper reviews recent progress on a new, simple, and powerful technique for ultrahigh-speed optical frequency-domain reflectometry (OFDR), namely, time-stretching (TS)-OFDR. This method is essentially based on the use of linear-dispersion-induced frequency-to-time mapping of the target broadband spectral interferogram so that this information can be captured in *real time* using a single photodetection stage and a fast analog-to-digital converter. The principle of operation, design tradeoffs, performance advantages, and limitations of TS-OFDR are discussed. Recent results on the application of TS-OFDR for fiber-optics device characterization and biomedical imaging are also presented.

Index Terms—Fourier transforms, frequency-domain analysis, optical interferometry, optical tomography, optical-fiber measurements, ultrafast optics.

I. INTRODUCTION

OPTICAL reflectometry [1]–[11] is an interferometric diagnosis method for a wide range of applications in, e.g., material, component and device characterization [1]–[3], [5], [7], [9], [12], [13], laser ranging and metrology [14], and biomedical tissue imaging [so-called optical coherence tomography (OCT)] [4], [10], [15]. OCT techniques can be divided into two main broad categories, namely, optical low-coherence reflectometry (OLCR) [1]–[4] and optical frequency-domain reflectometry (OFDR) [5]–[11]. As expected for an interferometry method, OLCR and OFDR offer increased spatial resolutions and sensitivities as compared with noninterferometry reflectometric techniques, e.g., optical time-domain reflectometry (OTDR) [16].

OFDR is based on the measurement of the target interference pattern in the frequency (wavelength) domain, in contrast to OLCR, where the interferometric signal is measured directly in the time domain, or equivalently, in the delay length domain. In OFDR, the measured spectral-domain information is typically converted into the desired length-domain information using discrete Fourier transformations (DFTs) with digital-signal processors. On the basis of their different operation principles, these two methods exhibit different performance tradeoffs in terms of axial depth range, spatial resolution, measurement speed, and sensitivity [17]–[19]. The performance limitations of OLCR are associated with the fact that a movable reference path needs to be implemented over an axial tuning range as long as the desired measurement depth range. Although one can translate the reference distance over a relatively long range (>1 m) [20], this inherently limits the measurement speed. OFDR enables overcoming these limitations since it only requires the measurement of an interference pattern in the spectral domain with a fixed reference path. In addition, it has been shown that an OFDR platform can provide an increased sensitivity in comparison with an OLCR system offering a similar spatial resolution and depth range [17]–[19]. Hence, OFDR has proved particularly advantageous for applications that require a combination of high speed, sensitivity, and resolution over short-to-intermediate depth ranges. Applications with these stringent requirements include characterization of fiber-optics and integrated-waveguide components and devices [12], and biomedical imaging [15].

In OFDR, the achievable spatial resolution depends inversely on the source spectral bandwidth (BW) (an improved spatial resolution requires the use of a larger spectral BW), whereas the measurement depth range is mainly determined by the spectral resolution in the interference-pattern measurement (a longer depth range requires a narrower spectral resolution). An OFDR system can be configured to achieve a variety of specifications, from submillimeter resolutions over depth ranges on the order of a few tens to hundreds of meters (e.g., for fiber-optics component characterization [12], [13]) to resolutions in the micron or even submicron regime over centimeter depth ranges (e.g., for biomedical OCT [15]). OFDR also offers a very high sensitivity, defined as the back-reflection level that produces a signal power equal to noise power, with experimentally demonstrated values well above -100 dB. A distinctive feature of OFDR

Manuscript received October 18, 2010; revised January 5, 2011; accepted January 27, 2011. Date of publication March 21, 2011; date of current version January 31, 2012. This work was supported in part by the Natural Sciences and Engineering Research Council of Canada, and in part by the Fonds Québécois de la Recherche sur la Nature et des Technologies and by the “Human Resource Development Center for Economic Region Leading Industry” Project from the Ministry of Education, Science and Technology (MEST) and the National Research Foundation of Korea (NRF).

T.-J. Ahn was with the Institut National de la Recherche Scientifique, Energie, Matériaux et Télécommunications (INRS-EMT), Varennes, QC J3X 1S2, Canada. He is now with the Department of Photonic Engineering, Chosun University, Gwangju 501-759, Korea (e-mail: taejung.ahn@chosun.ac.kr).

Y. Park was with the Institut National de la Recherche Scientifique, Energie, Matériaux et Télécommunications (INRS-EMT), Varennes, QC J3X 1S2, Canada. He is now with Automated Precision Inc., Rockville, MD 20850 USA (e-mail: kiywpark@gmail.com).

J. Azaña is with the Institut National de la Recherche Scientifique, Energie, Matériaux et Télécommunications (INRS-EMT), Varennes, QC J3X 1S2, Canada (e-mail: azana@mt.inrs.ca).

Color versions of one or more of the figures in this paper are available online at <http://ieeexplore.ieee.org>.

Digital Object Identifier 10.1109/JSTQE.2011.2112338

is that this outstanding performance can be achieved at very high measurement speeds. The diagnosis rate in interferometric measurements plays a fundamental role in many of the OFDR applications mentioned above. In the context of OCT biomedical imaging, fast acquisition rates are highly desired for *in vivo* screening of large tissues volumes, e.g., to enhance the quality of the reconstructed 2-D and 3-D images by reducing motion artifacts [21], [22]. Similarly, the ultrarapid characterization of components and devices is necessary for real-time monitoring of the characteristics of the target modules during fabrication or as they are operated within a given system [23].

The acquisition speed in an OFDR scheme is typically evaluated as the axial-line (A-line) scan rate, i.e., the inverse of the time period needed to capture the interferogram corresponding to a full single axial line. This rate is limited by the speed with which the interferometric signal spectrum can be recorded. One straightforward solution is to detect the individual spectral components of the interferogram separately by use of a spectrometer and a charge-coupled device (CCD) photodetection array [10], [17], [18]. The readout speed of current CCD arrays is too slow for applications requiring A-line scan rates in the kilohertz range and beyond. Spectrometer-based OFDR systems offering acquisition rates above 100 kHz have been recently reported by use of advanced ultrahigh speed CMOS photodetection arrays [24]. It has been shown that increased imaging speeds can be achieved by use of high-speed, wavelength-swept lasers combined with OFDR [19], [21], [22]. In this case, a single photodetection element, typically a balanced photoreceiver and a fast analog-to-digital converter (ADC), need to be employed to capture the spectral-domain interferogram information. The A-line scan rate is ultimately limited by performance of the wavelength-swept laser. Conventional CW wavelength-swept lasers usually consist of a broadband gain medium with a tunable optical bandpass filter in the cavity [25]. The wavelength-sweeping rate in these lasers is essentially limited by the intrinsic time constant for building up laser activity from spontaneous emission inside the cavity [25]. Essentially, the narrower the desired laser linewidth, the slower this scanning rate will be. To give a reference, a laser linewidth <1 MHz should be used for fiber-optics component characterization over an axial depth range approaching 100 m; current laser systems with such a narrow linewidth exhibit a relatively slow wavelength sweeping rate between 20–80 nm/s [12], [13]. State-of-the-art CW wavelength-swept lasers can be tuned over a BW >100 nm at a rate up to a few tens of kHz but at the expense of a relatively broad laser spectral linewidth (typically >10 GHz), corresponding to depth ranges of only a few millimeters [25]. This performance is perfectly well suited for OCT imaging applications [21], [22], in which the depth range is usually limited to a few millimeters by scattering losses in the analyzed tissue. In any case, higher imaging acquisition speeds, with A-line rates in the megahertz range, are still desired for a multitude of applications. In the context of OCT imaging, an innovative scheme for wavelength-swept lasers has been recently demonstrated, so-called buffered Fourier-domain mode-locking (FDML) method [26], [27]. This technique provides increased scanning rates on the order of hundreds of kilohertz or even

multimegahertz [28] over ultrabroad spectral BWs (>100 nm) with linewidths suitable for depth ranges >1 cm. FDML lasers are similar to conventional wavelength-swept lasers, except for the fact that the optical bandpass filter in the cavity is periodically tuned at the cavity round-trip time, or a harmonic of this period. Thus, FDML lasers are significantly more complex than conventional wavelength-swept lasers in terms of both implementation and operation. Regardless of the specific laser configuration, for high-sensitivity reflectometry applications, wavelength-swept lasers should exhibit a set of very stringent specifications, particularly in terms of high output power and low relative intensity noise (RIN) [12], [25]. Moreover, additional calibration and control mechanisms (typically, an additional interferometer [12], [29]) are usually necessary to accurately track the laser wavelength variation along the time.

The purpose of this paper is to review recent progress on a new technique for ultrahigh-speed OFDR [30]–[34], potentially capable of overcoming some of the above-discussed limitations of present OFDR methods. This novel technique, which will be here referred to as time-stretching OFDR (TS-OFDR), is based on the use of “temporal stretching” for mapping the spectral information into the time domain so that this information can be captured in *real time* using a single photodetection stage and a fast ADC [30]–[34]. Here, “real time” refers to the fact that the axial acquisition speed is as fast as the repetition rate of the input pulse source. This frequency-to-time mapping (FTM) is achieved in a completely passive fashion, i.e., by use of a large amount of linear chromatic dispersion (group-velocity dispersion, GVD) over a coherent ultrabroadband light interferogram. Frequency-to-time conversion of coherent light waves (optical pulses) using GVD [35] is usually referred to as “real-time optical Fourier transformation” (RT-OFT), and it can be interpreted as the time-domain equivalent of the process of far-field or Fraunhofer spatial-domain diffraction [36]. Briefly, a coherent broadband energy spectrum can be mapped along the time domain following linear propagation through a highly dispersive medium with predominant GVD (i.e., first-order dispersion). This simple but powerful concept has been extensively employed in the recent past for many applications, including real-time optical spectrum measurements [35], [36], temporal magnification of broadband waveforms for effectively increasing detection BW [37], high-frequency arbitrary microwave waveform generation [38], [39], real-time spectroscopy [40], 2-D imaging of rapidly changing physical processes [41], complex-field characterization of low-intensity ultrafast optical waveforms [42]–[45] with real-time and single-shot capabilities [46], and programmable optical pulse shapers with ultrahigh update rates [47]–[49]. Our review here addresses the use of RT-OFT for reflectometry applications (TS-OFDR) [30]–[34], [50]–[55] with a focus on recent results from our group at INRS-EMT.

In practice, TS-OFDR is implemented using an ultrabroadband optical pulse laser (i.e., mode-locked laser) as the seeding lightwave source. Concerning the required dispersive element, this can be implemented in a variety of practical ways, e.g., using fiber-optics technologies. To be more concrete, TS-OFDR has been demonstrated using (i) a long section of dispersive optical

fiber [30], [33], [34] or (ii) a more compact linearly chirped fiber Bragg grating (LCFG) operated in reflection [31], [32]. TS-OFDR offers several key advantages over wavelength-swept OFDR methods. First, as mentioned above, the interferogram associated with the object depth profile is obtained along the duration of a single temporally stretched optical pulse; as a result, the axial line (A-line) acquisition rate can be as high as the pulse repetition rate from the seeded optical source (up to a few tens of megahertz). Second, only a completely passive and linear pulse-stretching process (linear dispersion) is required as the wavelength sweep mechanism; this avoids the need for complex, active mechanisms for precise synchronous laser-wavelength tuning and calibration. Third, the peak power of the pulse incident upon the sample is effectively reduced by the input dispersion, which is also a potentially attractive feature to prevent damage in the tissues or components under test. Finally, the TS-OFDR setup is easy to be adapted for conventional OTDR for typical applications (e.g., range finder) because of the fact that these reflectometric setups consist of an ultrafast pulse source and high-speed data acquisition electronics. In turn, one can accommodate two independent reflectometry methods (i.e., TS-OFDR and OTDR) in a single fiber-optic platform.

TS-OFDR has already proved useful for a wide range of applications, particularly for fiber-optics and electrooptics (EO) component and device characterization. Some of these applications will be discussed in the following sections of our paper [50]–[53]. It has been also demonstrated that a TS-OFDR system can be configured to achieve the performance that is required for micrometer-resolution imaging applications over depth ranges in the centimeter regime [31]. However, due to the intrinsic dispersion-loss tradeoff of any dispersive element, TS-OFDR typically suffers from a relatively poor sensitivity. It has indeed proved difficult to reach the sensitivity level that is necessary for biomedical-imaging applications [30]–[33], at least better than -80 dB. We will discuss here how TS-OFDR can be optimized to potentially offer all the performance specifications, including sensitivity, that are required for biomedical-imaging applications [54], [55]. OCT images of a biological sample (onion) using a TS-OFDR system based on an LCFG are reported below.

The remainder of this review paper is structured as follows. The operation principle of the proposed reflectometry scheme (TS-OFDR) is described in Section II. In this section, we derive the expressions governing the performance specifications (axial resolution, depth range, and sensitivity) of a TS-OFDR scheme and discuss the practical tradeoffs and performance limitations and capabilities of the method. Many of the reviewed applications of TS-OFDR make use of an LCFG as the dispersive medium [31], [32]. The performance advantages and limitations of this solution as compared with the use of standard [30] or Raman-amplified [33] optical fiber sections are also briefly outlined in Section II. Results on applications of TS-OFDR for optical device characterization are reviewed in Section III, in particular real-time monitoring of group-delay characteristics of meter-long fiber-optics components [50], modal-delay measurements in high-order mode optical fibers [51], and real-time

complex-field temporal response characterization of high-speed (GHz BW) optical modulators [52], [53]. In Section IV, we report our most recent results on 2-D OCT imaging of a biological sample (onion) using a TS-OFDR system offering an axial resolution of ~ 40 μm and an improved sensitivity approaching -82 dB over a whole depth range (in air) of ~ 4.5 mm [54], [55]. Finally, we summarize and conclude our work in Section V. Future improvements and prospects of TS-OFDR are also discussed in this final section.

II. OPERATION PRINCIPLE OF TS-OFDR

A schematic of the necessary processing steps for implementing TS-OFDR [30], [31] is shown in Fig. 1. It consists of the following main subprocessing stages: coherent pulse generation; spectral broadening; dispersion-induced FTM; a conventional two-arm interferometer, and high-speed photodetection and sampling. TS-OFDR is based on the use of GVD-induced “temporal stretching” for mapping the spectral interference information along the time coordinate so that this information can be captured in *real time* using a single photodetection stage (either a single-ended photodetector or a balanced photodetector) and a fast electronic sampling circuit (ADC) [30]–[34]. The required time-mapped spectral interference pattern is obtained using a conventional two-arm interferometer (the fourth stage in Fig. 1). As detailed in the following theoretical analysis, the resulting temporal interference pattern is not an exact time-domain replica of the corresponding spectral interference: The spectral components of the chirped pulse from one of the interferometer arms are not coincidentally overlapped with the same spectral components of the interfering chirped pulse from the other arm (as it happens in the corresponding frequency-domain interference pattern), but with a frequency offset proportional to the optical path-length difference between the interferometer arms. Assuming that this optical path-length difference is made sufficiently large, this feature allows one to extract the desired differential phase information from the measured time-domain interference pattern using a simple DFT-based signal-processing algorithm [7]. In this way, the sample’s axial profile can be accurately recovered from the measured time-domain interferogram. It should be noted that an ultrabroadband energy spectrum is highly desirable for high-resolution OFDR and wideband characterization of photonic devices. In previous demonstrations of TS-OFDR [31], a spectral broadening method using self-phase modulation (SPM) in highly nonlinear fibers and a direct numerical compensation of the induced undesirable spectral phase distortions have been used. This spectral broadening is implemented after the coherent optical pulse generation (typically a mode-locked laser), as shown in Fig. 1.

A. Theoretical Analysis of TS-OFDR

Fig. 2 shows a schematic of the TS-OFDR technique, presenting the evolution of the involved time waveforms and corresponding spectra along the basic processing steps defined in Fig. 1. We assume that the second-order group-delay term (i.e., the GVD term) in the dispersive medium is dominant and sufficiently high. In our experiments described

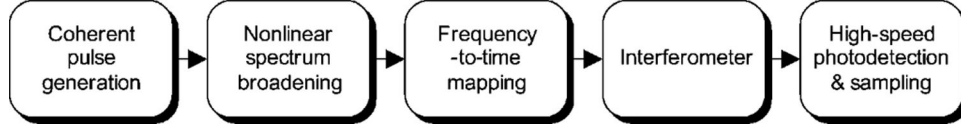


Fig. 1. Schematic of processing steps for implementing TS-OFDR.

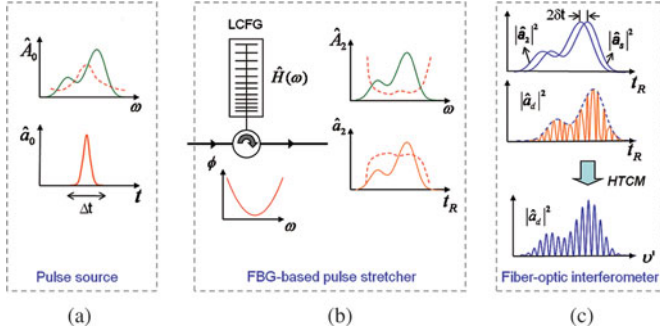


Fig. 2. Schematic diagram of optical and numerical processes in the proposed TS-OFDR technique, with the nomenclature defined in the text. In this illustration, the dispersive medium is assumed to be implemented using an LCFG operated in reflection.

below, a dispersion–compensation module made with a spool of dispersion–compensation fiber or an LCFG has been used as the FTM dispersive medium.

We define the input coherent pulse centered at the angular optical frequency ω_0 as an electromagnetic wave described by a temporal analytic function, a_0 , with a complex slowly varying envelope \hat{a}_0 , as shown in Fig. 2(a), i.e., $a_0(t) = \hat{a}_0(t) \cdot \exp(j\omega_0 t)$. The spectral transfer function of the dispersive medium can be mathematically described using the Taylor series expansion around ω_0

$$\hat{H}(\omega) = H_0 \exp\{-j\Phi(\omega)\} = H_0 \exp(-j\Phi_0 - j\dot{\Phi}\omega - j\frac{1}{2}\ddot{\Phi}\omega^2) \exp(j\delta\Phi) \equiv \hat{H}'(\omega) \exp(j\delta\Phi) \quad (1)$$

where $\Phi_0 = \Phi(\omega_0)$ is a phase constant, $\dot{\Phi} = [\partial\Phi(\omega)/\partial\omega]_{\omega=\omega_0}$ is the group delay, $\ddot{\Phi} = [\partial^2\Phi(\omega)/\partial\omega^2]_{\omega=\omega_0}$ is the first-order dispersion coefficient (GVD), and $\delta\Phi$ is the phase deviation (including higher order dispersion terms of the dispersive medium). The spectral phase of a predominantly first-order dispersive medium (e.g., LCFG) is shown in Fig. 2(b). The phase deviation $\delta\Phi$ is expected to be much smaller than the phase component of the main transfer function $\hat{H}'(\omega)$ along the entire spectral BW of interest. Note that in the above notation $\omega = \omega_{\text{opt}} - \omega_0$, where ω_{opt} is the optical frequency variable and ω is the baseband frequency variable. It is well known that the impulse response corresponding to the transfer function $\hat{H}'(\omega)$ can be written as [36]

$$\hat{h}(t_R) = h_{\text{time}} \exp\left(j\frac{1}{2\ddot{\Phi}}t_R^2\right) \quad (2)$$

where $t_R = t - \dot{\Phi}$ and $h_{\text{time}} = H_0 \exp(-j\Phi_0)/\sqrt{j2\pi\ddot{\Phi}}$. In this time-invariant linear system, the spectrum of the reflected wave, $\hat{A}_2(\omega)$, and that of the input wave $\hat{A}_0(\omega)$ can be related

as follows:

$$\begin{aligned} \hat{A}_2(\omega) &= \hat{H}(\omega) \cdot \hat{A}_0 = \hat{H}'(\omega) \cdot \exp(j\delta\Phi) \cdot \hat{A}_0(\omega) \\ &\equiv \hat{H}'(\omega) \cdot \hat{A}_1(\omega) \end{aligned} \quad (3)$$

where the phase deviation of the dispersive medium from its ideal characteristics is included in the “intermediate” pulse spectrum $\hat{A}_1(\omega) = \hat{A}_0(\omega) \cdot \exp(j\delta\Phi) = |\hat{A}_0(\omega)| \cdot \exp[j(\phi + \delta\Phi)]$, $\phi(\omega)$ being the spectral phase profile of the input optical pulse \hat{a}_0 . The corresponding time-domain expression of (3) is as follows: $\hat{a}_2(t_R) = \hat{a}_1(t_R) * \hat{h}(t_R)$, where \hat{a}_1 and \hat{a}_2 are the inverse Fourier transforms of \hat{A}_1 and \hat{A}_2 , respectively. We now calculate the convolution integration in order to look into the time-domain evolution of the input pulse as it propagates through the dispersive medium. In fact, if the total time duration Δt_1 of the pulse waveform $\hat{a}_1(t_R)$ is sufficiently short such that the following condition is satisfied [36]:

$$\left| \frac{\Delta t_1^2}{8\pi\ddot{\Phi}} \right| \ll 1 \quad (4)$$

then the convolution integral can be approximated by the following expression [31], [36]:

$$\begin{aligned} \hat{a}_2(t_R) &\approx h_{\text{time}} \exp\left(j\frac{1}{2\ddot{\Phi}}t_R^2\right) \{\mathfrak{F}[\hat{a}_1(t_R)]\}_{\omega'=t_R/\ddot{\Phi}} \\ &= h_{\text{time}} \exp\left(j\frac{1}{2\ddot{\Phi}}t_R^2\right) \hat{A}_1(\omega') \end{aligned} \quad (5)$$

where \mathfrak{F} denotes the Fourier transform and $\omega' = t_R/\ddot{\Phi}$ is the transformed frequency variable, which is scaled by the first-order dispersion term. Note that, in practice, the phase-deviation factor $\delta\Phi$ is typically small and one can safely assume that $\Delta t_1 \approx \Delta t$, where Δt is the total time duration (full time width) of the input pulse waveform $\hat{a}_0(t)$. Equation (5) indicates that under the conditions of (4), the amplitude spectrum of the input optical pulse is efficiently mapped along the time domain following propagation through the highly dispersive element. The inequality in (4) is usually referred to as the temporal Fraunhofer condition [36]. A detailed derivation of (4) and (5) can be found in Appendix I.

Similarly, the reflection of the stretched optical pulse $\hat{a}_2(t)$ from a sample is assumed to be approximated by the convolution of this pulse with the characteristic temporal impulse response, $\hat{f}(t_R)$, of the sample in the moving time frame, t_R . Note that the function $\hat{f}(t_R)$ is proportional to the target sample (amplitude and phase) depth profile with a finite frequency BW restricted by the BW of the input light source. In the frequency domain, the waveform reflected from the sample can be expressed as follows:

$$\hat{A}_s(\omega) = \hat{F}(\omega) \cdot \hat{A}_2(\omega) = \hat{H}'(\omega) \cdot [\hat{F}(\omega) \cdot \hat{A}_1(\omega)] \quad (6)$$

where \hat{F} is the spectral transfer function corresponding to the sample time impulse response, i.e., $\hat{F}(\omega) = \mathfrak{F}\{\hat{f}(t_R)\}$. The temporal representation of (6) can be similarly approximated as in [31] and [36] by

$$\begin{aligned} \hat{a}_2(t_R) &\approx h_{\text{time}} \exp\left(j\frac{1}{2\ddot{\Phi}}t_R^2\right) \left\{ \mathfrak{F}\left[\hat{a}_1(t_R) * \hat{f}(t_R)\right] \right\}_{\omega'=t_R/\ddot{\Phi}} \\ &= h_{\text{time}} \exp\left(j\frac{1}{2\ddot{\Phi}}t_R^2\right) \hat{A}_1(\omega') \hat{F}(\omega'). \end{aligned} \quad (7)$$

Following a similar derivation to that used for (4) and (5) (see Appendix D), one can easily show that the approximation in (7) is strictly valid when the temporal Fraunhofer condition $|\Delta t_3^2/8\pi\ddot{\Phi}| \ll 1$ is satisfied, where Δt_3 is the full time width of the pulse waveform $\hat{a}_3(t_R) \approx \hat{a}_1(t_R) * \hat{f}(t_R)$. In most cases, the time width Δt_3 is approximately given by the duration of the sample's temporal impulse response $\hat{f}(t_R)$ and this latter condition is indeed more restrictive than the inequality in (4). This constraint may affect the maximum depth range that can be achieved for a given GVD value; however, in practice, the depth range is usually limited by the photodetection BW. Detailed discussions on this issue can be found below in Section II-C. Also note that whereas the GVD must be sufficiently large to satisfy the above-stated temporal Fraunhofer conditions, overlapping between the successive temporally stretched waveforms, repeating at the nominal repetition rate of the mode-locked laser, should be avoided. This imposes a limitation on either the maximum GVD or the maximum repetition rate of the pulsed laser. These additional constraints are also discussed below in Section II-C.

Equation (7) implies that the sample transfer function is *replicated* along the duration of the stretched pulse when this pulse is backscattered and/or reflected from the sample. In other words, the sample spectral transfer function (in amplitude or intensity) can be directly captured in the temporal domain by simply measuring the time intensity envelope of the waveform reflected from the sample. Employing coherent interference of the sample-reflected pulse with a reference pulse (properly delayed input stretched waveform), $\hat{a}_2(t_R - 2\delta t)$, where $2\delta t$ is the relative time delay in a Michelson interferometer (see Fig. 2), one can also recover the desired information on the phase profile of the sample spectral transfer function. In particular, using the expressions for the input stretched waveform $\hat{a}_2(t_R)$ in (5) and the sample-reflected waveform $\hat{a}_s(t_R)$ in (7), the corresponding temporal intensity pattern at the interferometer output can be expressed as follows:

$$\begin{aligned} |\hat{a}_d(t_R)|^2 &\propto |\hat{a}_s(t_R) + \hat{a}_2(t_R - 2\delta t)|^2 \approx |h_{\text{time}}|^2 \\ &\quad \cdot (I_{\text{DC}} + I_{\text{AC}} + I_{\text{AC}}^*) \\ I_{\text{DC}} &\equiv |\hat{A}_1(\omega') \hat{F}(\omega')|^2 + |\hat{A}_1(\omega' - \Omega)|^2 \\ I_{\text{AC}} &\equiv |\hat{A}_0(\omega')| \cdot |\hat{A}_0(\omega' - \Omega)| \cdot \hat{F}^*(\omega') \\ &\quad \cdot \exp[-j(2\omega'\delta t + \Delta\phi(\omega'))] \\ \Delta\phi(\omega') &\equiv \phi(\omega') - \phi(\omega' - \Omega) + \delta\Phi(\omega') - \delta\Phi(\omega' - \Omega) \end{aligned} \quad (8)$$

where $\Omega \equiv 2\delta t/\ddot{\Phi}$ is the frequency shearing induced by the time delay, $2\delta t$, in the frequency-to-time converted coordinate and where we recall that ϕ represents the spectral phase profile of the input optical pulse. The first term, I_{DC} , on the right-hand side of the above equation is considered as a dc term composed by two contributions, namely, the power spectra of the pulse reflected from the sample and of the reference. The second and the third terms, I_{AC} and I_{AC}^* are the interference terms from which one can directly reconstruct the complex impulse response $\hat{f}(t_R)$ of the sample under test by use of a conventional DFT-based numerical algorithm [7].

To conclude this section, it should be mentioned that whereas our analysis has been carried out by assuming that the dispersive device is located before the interferometer, these two blocks can be interchanged in a practical system, i.e., the dispersive device can be located immediately after the interferometer, leading to identical results to those derived above. The use of dispersion before the interferometer guarantees that the optical pulse reaches the sample with a lower peak power, which may help reducing potential damage in the target (e.g., biological tissue). In contrast, it has been proved that by locating the dispersive device after the interferometer, one can minimize or fully avoid detrimental Doppler frequency shifts induced by sample movements [32], [34]. This is due to the fact that in this case, the interaction time between the optical pulse and the target is significantly decreased.

B. Phase Distortion Compensation for Optimal Axial-Line Resolution

In order to achieve an optimal reconstruction of the sample impulse response, the differential spectral phase factor $\Delta\phi(\omega')$ must be properly compensated for. We recall that this detrimental phase factor includes the high-order dispersion terms of the employed dispersive element (this includes group-delay ripples, GDR, in an LCFG), and the nonlinear spectral phase profile of the input optical pulse. Note that the nonlinear spectral phase generally induced by the nonlinear fiber to achieve the desired pulse spectral broadening for high axial resolution should be also compensated for. A schematic of the recorded interferogram in the TS-OFDR technique is shown in Fig. 2(c). As evidenced by (8), if uncompensated, this differential phase factor may significantly affect the axial resolution of the recovered sample depth profile. In our work, we have used a simple and direct numerical technique for compensating for the above mentioned phase distortions which is based on predetermining the precise time-to-frequency mapping (TFM) to be applied over the measured time-domain spectral interferograms [29], [31]. The core of this technique is to obtain the differential spectral phase factor, $\Delta\phi(\omega')$, by simply acquiring the interference pattern $|\hat{a}_d(t_R)|^2$ in (8) from a single reflection point, i.e., when $\hat{F}(\omega') = \text{constant}$, and applying the so-called Hilbert transformation (HT) compensation method (HTCM) [29]. In this method, the complex ac interference component, I_{AC} , can be obtained from the measured interference pattern using the following procedure. The HT is only applied on the ac part. We are assuming that the ac interferogram is a causal signal, which

enables application of the HT for recovering the imaginary part of the signal. The definition and other details of the HT can be found in Appendix II (see Table I). First, the real part of the ac interference component can be directly extracted from the measured interference pattern, $I_{AC} + I_{AC}^* = \text{real}(I_{AC})$, by numerically subtracting the dc component or by simply detecting the signal with a dual-balanced photoreceiver [54]. In practice, this subtraction can be easily performed by numerically filtering the Fourier transform of the measured temporal interference pattern with a narrow bandpass filter.

The phase variation of the ac waveform is given by the differential spectral phase factor $\Delta\phi(\omega')$ (see (8) with $\hat{F}(\omega') = \text{constant}$). This phase factor $\Delta\phi(\omega')$ can thus be easily obtained from the extracted interference pattern. In particular, considering that the real and imaginary parts of the complex ac pattern are related by the HT [29]

$$\Delta\phi(\omega') = 2\omega'\delta t + \Delta\varphi(\omega') = \tan^{-1} \left[\frac{\text{imag}\{I_{AC}\}}{\text{real}\{I_{AC}\}} \right] \quad (9)$$

where we recall that $2\delta t$ is the relative time delay in a Michelson interferometer. A minimum delay requirement in the interferometer for HT is the time delay to obtain a sinusoidal interferogram with at least a single period, similarly to conventional implementations of spectral interferometry.

From the calculated differential phase factor $\Delta\Phi$, the numerical TFM to be applied over the measured interference patterns can be precisely recalibrated as follows:

$$\omega'' = \frac{\Delta\Phi(\omega')}{2\delta t}. \quad (10)$$

It is worth mentioning that in order to ensure that the differential phase factor $\Delta\phi(\omega')$ is accurately extracted, the relative delay between the interfering waveforms $2\delta t$ must be sufficiently large so that to ensure that the corresponding frequency shifting $\Omega \equiv 2\delta t/\ddot{\Phi}$ is larger than the frequency resolution $\delta\omega_1$ of the spectral waveform under analysis $\hat{A}_1(\omega')$. Mathematically, $\Omega = 2\delta t/\ddot{\Phi} > \delta\omega_1$, where $\delta\omega_1 \sim 2\pi/\Delta t_1$, and we recall the reader that Δt_1 is the full time width of the waveform under analysis $\hat{a}_1(t_R)$. The resulting condition $\delta t \cdot \Delta t_1/\pi\ddot{\Phi} > 1$ necessarily implies that the used GVD is not sufficient to induce FTM of the entire two-pulse interference waveform, $\hat{a}_d(t_R) \propto \hat{a}_1(t_R) + \hat{a}_1(t_R - 2\delta t)$, but only of each one of the single pulse waveforms separately [as ensured by the condition in inequality (4)]. Thus, we reiterate that the obtained temporal interference pattern is not a time-domain replica of the corresponding spectral interference profile. Indeed, the spectral interference profile $|\hat{A}_d(\omega)|^2 \propto |\hat{A}_1(\omega) + \hat{A}_1(\omega) \exp(j2\omega\delta t)|^2$ contains no information at all on the phase difference (group delay) of the waveform of interest.

Note that, in practice, the presented compensation method can be used for simultaneously correcting the phase distortions induced by dispersion unbalance in the fiber interferometer. However, this phase correction for dispersion unbalance holds only over a narrow depth range centered at $2c\delta t$, and application of the correction outside this range causes significant blurring of the reconstructed depth profile [55].

The presented calibration method enables to retrieve very precisely the time versus frequency curve of the used dispersive element, namely, its group-delay response. As a result, this simple and practical method itself can be exploited for highly accurate characterization of the group-delay response of dispersive devices. The use of this idea for fast (real time) group-delay characterization of ultrabroadband fiber-optics dispersive elements, in particular ultralong LCFGs, is discussed in Section III-A below as one of the many interesting applications of TS-OFDR.

C. Performance Tradeoffs of TS-OFDR

1) *Axial Resolution*: As in conventional OFDR, the axial resolution that can be achieved with TS-OFDR essentially depends on the input pulse optical BW and central wavelength [21]. Assuming that the optical BW of the input pulse is $\Delta\lambda_S$ [in nanometers], the optimal (transform-limited) axial resolution can be estimated as [21]

$$\delta z \approx 0.44 \frac{\lambda_0^2}{\Delta\lambda_S} \quad (11)$$

where λ_0 is the center wavelength of the pulse source and here, the pulse spectrum is assumed to be Gaussian-like. When using an LCFG as the dispersive medium, (11) holds as long as the input pulse spectrum is narrower than the reflection BW of the grating. If the input optical BW is larger than the LCFG reflection BW, $\Delta\lambda_{\text{LCFG}}$ (in nanometers), then the system axial resolution will be limited by the LCFG BW. A more accurate estimation of the corresponding axial resolution in this case is given by the following expression [15]:

$$\delta z \approx 0.66 \frac{\lambda_0^2}{\Delta\lambda_{\text{LCFG}}} \quad (12)$$

which is obtained by assuming that the spectral amplitude transmission profile of the LCFG is approximately rectangular (as it is usually the case). Utilizing the full BW of an LCFG with a ~ 42 -nm full-reflection BW, centered around 1545 nm, we achieved axial resolutions down to 42 μm , in good agreement with the prediction from (12).

2) *Axial Depth Range*: As discussed in previous works, the free-space depth range of an OFDR system essentially depends on the resolvable spectral linewidth in the system [21], [30] (a longer depth range can be achieved by narrowing the resolvable spectral linewidth). In what concerns a TS-OFDR system, this spectral linewidth essentially depends on the amount of GVD introduced by the dispersive element (i.e., stretching rate) and may be limited by either the range of validity of the corresponding temporal Fraunhofer condition $|\Delta t_3^2/8\pi\ddot{\Phi}| \ll 1$ (to ensure FTM of the filtered sample's time impulse response, $\hat{a}_3(t_R)$) or by the photodetector BW. To evaluate which contribution becomes more important in a practical case, we performed numerical simulations without assuming a priori the validity of the Fraunhofer approximation. In these simulations, we considered a purely first-order dispersive element with a GVD of 2000 ps/nm (similar to the GVD used in our previously reported TS-OFDR experiments [31]); no phase deviations were assumed to simplify the analysis. The DFTs of the given

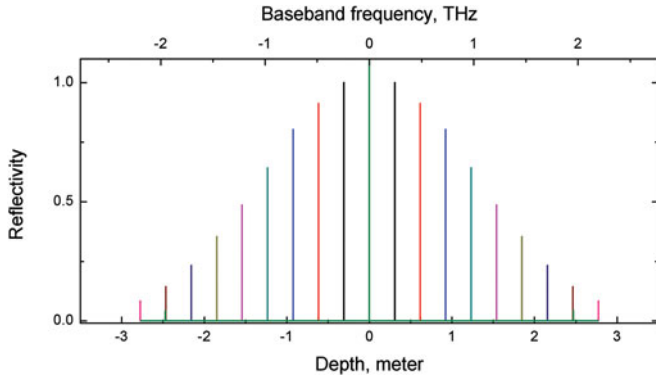


Fig. 3. Roll-off of the axial reflections for evaluating the optical spectral resolution in TS-OFDR without considering the finite photoreceiver BW.

dispersed signal $\hat{A}_s(\omega)\hat{H}(\omega)$ and the dispersed reference spectrum $\hat{A}_2(\omega - \Omega)\hat{H}(\omega)$ are proportional to the FTM fields of the two spectra. Their superposition and absolute square represent the temporal interference intensities. As expected, unlike the ideal case in (8), the interference fringes will exhibit a limited contrast as the position of the sample relative to the reference (i.e., as the duration of the sample's temporal impulse response) is increased due to the finite resolution of the FTM process. The absolute square of the inverse Fourier transform of the resulting intensity waveform provided the depth reflection profile with a roll-off as the time delay was increased. To evaluate the optical limitation on the depth range, we did not consider the finite photoreceiver BW. Fig. 3 shows the reflection roll-off with respect to the reflection depth from the target. A Gaussian spectral shape source centered at 1550 nm and with a BW of 10 nm [full-width at half-maximum (FWHM)] was assumed for the simulation. According to this simulation, the depth range corresponding to a signal attenuation of ~ 10 dB is nearly 3 m. It can be easily shown that in most of practical cases, the depth range limitation imposed by the finite photoreceiver BW (~ 10 to 50 mm in our examples) is much more severe than this simulated depth range restriction.

Thus, in practice, the free-space depth range will be limited by the photodetector BW, according to the following approximate expression [31]:

$$\Delta z \leq \frac{1}{4} \lambda_0^2 |\ddot{\Phi}_\lambda| \text{BW} \quad (13)$$

where $\ddot{\Phi}_\lambda = -(2\pi c/\lambda_0^2)\ddot{\Phi}$ is the GVD of the dispersive element expressed in (in picosecond per nanometer) units.

The equations derived above reveal that in a TS-OFDR system there is a fundamental tradeoff between the achievable axial resolution and depth range. Basically, a longer depth range can be obtained by use of a higher amount of dispersion. However, the higher the dispersion introduced by the pulse-stretching system, the narrower the input pulse BW must be in order to avoid temporal overlapping among the stretched optical pulses (to maintain the same input pulse repetition rate) and this necessarily implies a poorer spatial resolution.

3) *Sensitivity*: As discussed in [21] for a wavelength-swept OCT system, the sensitivity is inversely proportional to the de-

tor BW and as a result, the optimum detection BW will depend on the wavelength tuning rate (the detection BW should be as narrow as possible still to be able to follow the predefined tuning rate). In our approach, the optimum detection BW can be similarly approximated by $\text{BW} \approx 0.4 N_s / (\ddot{\Phi}_\lambda \Delta \lambda_{\text{LCFG}})$, where N_s is the sampling number. Hence, the optimum BW is inversely proportional to the dispersion-BW product of the LCFG, which, in turn, is inversely proportional to the wavelength tuning rate in the OFDR system. In other words, as expected for a wavelength-swept OCT system, the optimum BW is directly proportional to the wavelength tuning rate. Note that this expression is derived from a direct application of the Nyquist criterion, assuming that the sampling BW is 2.5 times wider than the detector BW.

With a single-ended photodetection scheme [30], [31], intensity noise from the stretched pulses was the dominant source responsible for the achieved poor sensitivity (61 dB). In a recent work, the sensitivity of a TS-OFDR system has been further improved up to -68 dB by the use of a digital normalization detection technique [56]. In bioimaging applications, this sensitivity level is still not sufficient for imaging a biological sample, considering that 10^{-8} to 10^{-9} of the input optical power is typically back-reflected from biological samples. The maximum achievable sensitivity ever reported using a TS-OFDR has been -82 dB using a high-speed balanced photoreceiver [54]. This sensitivity has enabled the use of TS-OFDR for OCT imaging of biological samples [54], [55]. These results will be discussed in further detail in Section IV below. Electrical amplifier noise has been identified as the main limiting factor in our experimentally demonstrated OCT system.

4) *A-Line Rate and Update Rate*: As discussed above, the depth-line profile acquisition rate (“A-line rate”) can be as high as the pulse repetition rate since the FTM takes place in a pulse-by-pulse basis. In our previous experiments, we achieved A-line rates as fast as 20 M-lines/s [31]. However, it should be mentioned that the pulse repetition rate has to be lowered if the pulse time period (T_R) is shorter than the time duration of the FTM pulse (i.e., pulse after the dispersion) in order to prevent temporal overlapping between neighboring pulses. The use of a wider input pulse spectrum $\Delta \lambda_S$ (i.e., for an improved axial resolution) imposes the need to lower down the input pulse repetition rate. Thus, there is a fundamental limit for the maximum A-line rate determined by the FTM pulse duration, in particular, $T_R \geq \ddot{\Phi}_\lambda \Delta \lambda_S$.

It is also important to mention that the A-line rate is not equivalent to the continuous update rate of the reconstructed axial depth profile that the system can actually provide. Here, the “update rate” is defined as the speed at which the reconstructed depth profile (or image) can be displayed. In TS-OFDR, the update rate is not limited by the optical realization of the FTM but by the performance of the ADC stage. Compared to the A-line rate, the line-by-line update rate is typically much lower due to the standard long lead time to grab a new waveform in a high-speed ADC. Using a high performance ADC, a continuous capture rate can be achieved up to ~ 10 kHz [57]. For 2-D imaging, one may need to use a long on-board memory to grab and store a multitude of consecutive axial lines while scanning along the transversal direction.

D. Performance Advantages and Limitations of an LCFG

The use of a highly dispersive LCFG, i.e., a fiber Bragg grating where the perturbation period is linearly increased (or decreased) along the device length, as the dispersive element in a TS-OFDR scheme [31], [32], instead of a long section of optical fiber [30], [33], offers a number of critical advantages. An LCFG allows stretching optical pulses with a much higher input peak power than in an equivalent optical fiber scheme. This is associated with the fact that an LCFG can provide a very high dispersion in significantly more compact forms than conventional optical fibers. For instance, the dispersion introduced by the 10-m-long LCFG used in our previously reported experiments [31] is equivalent to that of ~ 120 km of conventional SMF fiber, i.e., equivalent to a dispersion-compensation fiber with a length of at least a few kilometers. In a long dispersive optical fiber, the input pulse may need to be strongly attenuated to avoid nonlinear optical wave breaking and additional unwanted nonlinear effects. A high input peak power is, however, desired in OFDR to be able to improve both the system sensitivity and the axial depth range [21]. In relation with this, an LCFG can be designed to achieve a nearly 100% reflectivity over the desired operation BW, and as a result, the insertion losses of the device are mainly due to the need to operate the device in reflection [58]. Insertion losses lower than 1 dB can be easily achieved by use of an optical fiber circulator to retrieve the reflected signal from the LCFG. In contrast, in a dispersive optical fiber, the insertion loss increases with the fiber length, i.e., a higher dispersion necessarily implies an increased insertion loss. These losses can be compensated for by use of amplification. For this purpose, the use of distributed Raman amplification in a dispersion-compensating fiber module has proved particularly advantageous [33]. Nonetheless, the use of amplification introduces an additional source of noise which may have a negative effect on the OFDR system performance, especially on the system sensitivity.

As another advantage, a fiber Bragg grating (e.g., LCFG) can be specifically designed to achieve a desired group-delay curve (e.g., linear group delay) over a prespecified BW; thus, these two specifications (dispersion and BW) can be independently customized in the fiber grating device according to the targeted system requirements [58]. It is worth noting that previous theoretical analysis and experimental studies have revealed that a high, *linear* pulse-stretching rate is essential to achieve a *uniform* sensitivity and resolution over a longer depth range [31], [32]. An LCFG can provide the desired nearly linear group delay over a very broad BW. Specifically, LCFG technology has evolved to the point that several meters long, high-quality gratings can be readily fabricated [59]. This should easily allow scaling the technique for operation over input pulse BWs > 100 nm. In contrast, it would be extremely challenging to obtain a linear group delay over such broad BWs using a long section of conventional SMF or dispersion-compensation optical fiber.

It should be also mentioned that an LCFG can be used from its two ends to introduce the same amount of GVD but with two opposite dispersion signs. This unique feature of an LCFG could be potentially exploited for a range of additional processing applications. In a relevant example, this property has been

successfully used for decoupling movement-induced Doppler frequency shifting information from the desired range profiling information in a TS-OFDR system [32].

Finally, we note that a potentially important limitation of an LCFG is that this device typically exhibits pronounced reflectivity ripples and GDRs [58]. While the effect of reflectivity ripples can be easily compensated for in the numerical-data-analysis stage, the influence of GDR has proved more detrimental and challenging to deal with, e.g., in the context of dispersion-compensation applications [63]. In our OFDR systems, we have employed an advanced numerical procedure based on the HT to extract the precise TFM in the system; this procedure, which is described in detail in section II.B above, allows one to compensate for the phase distortions introduced by the GDR of the LCFG device, thus significantly minimizing the effect of these ripples on the system performance.

III. PHOTONIC DEVICE CHARACTERIZATION BY TS-OFDR

A. Real-Time Group-Delay Measurement of Ultra Broadband Dispersive Devices

The phenomenon of linear chromatic dispersion is of fundamental importance in many different fields, including high-bit-rate fiber-optics telecommunications [60], ultrashort optical pulse generation and ultrafast optical signal processing [61]. Chromatic dispersion is mainly characterized through the group-delay response of the involved medium or device. Thus, precise characterization of the group-delay response of dispersive devices is a critical functionality in all the above fields. TS-OFDR has demonstrated to be particularly useful for this important application [50].

As a practically relevant example, group-delay measurements are required for precise characterization of dispersion-compensation modules, i.e., devices devoted to compensate for the dispersion induced by propagation through fiber-optics communication links [60]. In particular, LCFG technology has recently attracted considerable attention for its application as a dispersion-compensator in optical communication systems, allowing to overcome the main drawbacks (i.e., signal distortion induced by fiber nonlinearities, large insertion losses, and bulkiness) of the conventional dispersion-compensating fiber solution [62]. However, the GDR of the LCFG, which mainly results from imperfections in the grating period, may significantly degrade the performance of LCFG-based dispersion-compensators [63] especially for ON-OFF-keying data rates ≥ 40 Gb/s in optical networks. To efficiently suppress the GDR, a fast and precise GDR measurement technique is required to be able to monitor the GDR faster than the instantaneous process time necessary for GDR reduction. The conventional wavelength-swept OFDR technique provides unparalleled performance in terms of measurement speed and measurable device length (e.g., 4 Hz over a 2 nm BW for devices up to 70 m long [12], [13]); however, the OFDR performance is intrinsically limited by the need for a stable narrowband wavelength tuning mechanism over the whole measurement spectral BW. Thus, we have proposed the use of TS-OFDR for group-delay

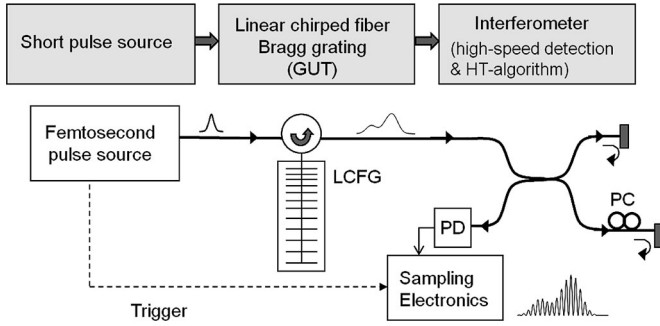


Fig. 4. Schematic concept diagram of the TS-OFDR-based GDR measurements of an LCFG; GUT: grating under test.

measurements of dispersive devices and more in particular, for GDR characterization of LCFGs. This simple and powerful scheme has been shown to be particularly advantageous for characterizing ultralong LCFGs as it does not exhibit a fundamental limitation on the measurable device length while having the potential to provide unprecedented measurement speeds (megahertz range). In addition, the TS-OFDR method offers high measurement accuracy due to the fact that it is based on the use of a very stable mode-locking optical pulse source and a very simple passively wavelength-swept interferometric setup without involving any mechanical delay line or wavelength sweeping element. It can be also extended to achieve real-time GDR monitoring in combination with high-speed data acquisition modules (real-time scope or ADC) [64].

A schematic concept diagram of the operation principle is shown in Fig. 4. The proposed group-delay measurement technique applies the above-described HTCM procedure for extracting the differential spectral phase [defined as $\Delta\phi(\omega)$ in (8)] from the measured TS-OFDR interferogram. A single-point reflection (mirror) is used as the “sample” and the element (LCFG) to be tested is employed as the dispersive medium inducing the FTM process in the TS-OFDR scheme: During the pulse dispersion process, the reflectivity ripple and GDR of the LCFG will be then mapped into the amplitude and phase temporal profiles of the stretched pulse, respectively. The stretched pulse, which includes the phase variation caused by higher order dispersion and GDR of the LCFG, is launched into a simple fiber-optic interferometer and the temporal interferogram is subsequently acquired by a high-speed detection system. Note that we ignore the phase of the used short pulse source in the measurement because it is assumed to be nearly transform-limited. The GDR can then be accurately recovered from the self-interference temporal intensity pattern of this stretched pulse by using the HT-based phase reconstruction method (HTCM) described above in Section II-B. In this scheme, the measurable wavelength region is determined by the spectral BW of the input coherent optical pulse.

Assuming that the dispersion of the LCFG under test is sufficiently high, the stretched pulse after reflection from this LCFG can be expressed as $\hat{a}_1(t) \propto \exp(jt^2/2\ddot{\Phi}_0) \hat{A}_0(\omega') \exp(-j\delta\Phi)$, where $\omega' = t/\ddot{\Phi}_0$ is the transformed frequency, scaled by the LCFG first-order dispersion term $\ddot{\Phi}_0$ [31].

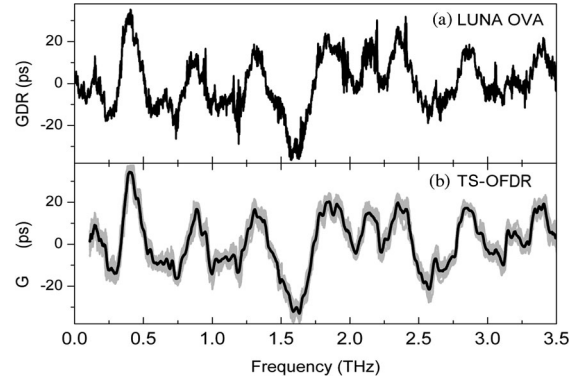


Fig. 5. GDRs of the LCFG measured by (a) LUNA optical vector analyzer and (b) TS-OFDR-based method with 15 times averaging process. Gray zone shows the overlapped plots with an averaged data line (from [50]).

In this transformation, one can easily recognize that the amplitude $|\hat{a}_1(t)|$ of the stretched pulse is directly proportional to the input pulse spectrum, $|\hat{A}_0(\omega')|$, whereas the phase of the stretched time waveform consists of the input pulse spectral phase and the quadratic phase profile induced by the first-order dispersion (GVD, $\ddot{\Phi}_0$) and higher order phase terms ($\delta\Phi$) of the LCFG. The phase information of the LCFG can be accurately recovered from the recorded interference temporal pattern by applying the HTCM [31]. In particular, the time-varying instantaneous frequency, $\nu(t)$, induced by the LCFG can be precisely recovered from the calculated differential phase factor $\Delta\Phi$ using the following relationship $\Delta\Phi(t) = (2\pi nL/c)\nu(t)$, where L is the round-trip length difference between the two arms of the Michelson interferometer, n is the refractive index, and c is the speed of the light in vacuum. The recovered instantaneous frequency can be reciprocally expressed by $\tau(\nu)$, which represents the group-delay curve (as a function of the optical frequency) of the LCFG under test. This procedure is valid as long as the group-delay curve is a single-value function. Finally, the GDR can be obtained by subtracting the second-order polynomial fitting curve from the measured group-delay function (i.e., both first and second-order dispersion are subtracted).

As a proof-of-concept experiment, we have measured the GDR of a 10-meter long LCFG ($\sim +2000$ ps/nm, Proximion, Inc.) placed prior to the interferometer in the setup (see Fig. 4). We used a passively mode-locked fiber laser (FFL, Pritel, Inc.) generating nearly transform-limited Gaussian-like optical pulses with a FWHM time duration/spectral BW of ≈ 0.5 ps/8 nm and an average power of 390 μ W at 20 MHz repetition rate. The input pulses were stretched to ≈ 16 ns by the LCFG, which induced the anticipated FTM process. A simple fiber-optic Michelson interferometer was employed to generate a single temporal interferogram for the phase recovery process. The temporal interferogram was acquired by a high-speed photoreceiver with 20 GHz BW (Tektronix 80C01) mounted in a sampling oscilloscope (Tektronix CSA8000). Fig. 5(a) shows the GDR profile of the LCFG measured by means of a commercial optical vector analyzer (OVA, LUNA Technology, Inc.) based on conventional wavelength-sweep OFDR [12], and Fig. 5(b) shows the GDR profile of the LCFG measured by the

TS-OFDR method. In Fig. 2(b), the gray zone shows the overlapped plots from fifteen different, consecutive measurements, whereas the black curve is the fifteen-times averaged data line. Our measured GDR curve is very consistent with the single-shot measurement result obtained from the LUNA OVA. In our measurement, a maximum standard deviation (SD) of 3.89 ps was achieved; this compares favorably with the 12.38-ps SD of the provided data [this relatively high SD is mainly associated with the unexpected abrupt peaks observed in the high-wavelength-resolution GDR curve measured by the commercial OVA; see Fig. 5(a)]. The high accuracy offered by our proposed technique is mainly due to two reasons: (i) the pulse source provides very high quality and time-stable signals and (ii) the wavelength sweep has been realized by an entirely passive mechanism. In addition, an unprecedented GDR monitoring rate of ~ 5 frames/s has been recently demonstrated using this technique in combination with a commercial 8-Gsamples/s real-time oscilloscope operating as an ultrafast digitizer to capture and process the temporal interferograms [64]. As discussed above, the wavelength resolution in this TS-OFDR measurement scheme could be improved by adding a well-characterized pulse stretcher in series with the LCFG under test; this may however require reducing the input pulse repetition rate (i.e., measurement update rate).

B. Modal Delay Measurement for Higher Order Mode Fibers Based on TS-OFDR

Multi-mode fibers, and more in particular so-called higher order mode fibers (HOF), continue attracting considerable research interest due to the extraordinary dispersion and nonlinear characteristics of the higher order modes in these fibers [65]–[67]. HOF technology has been used for dispersion-compensators [65], dispersionless bandpass filters [66], and variable optical attenuators [67]. In general, the excited modes in an HOF can be separated in time owing to their group velocity differences. A simple time-domain method based on time-of-flight measurement of a propagating ultrashort optical pulse has proved very useful to determine the modal delays between the different excited modes in an HOF [68]. However, the temporal resolution of this method, which depends on the input pulsewidth and the detector BW, limits the minimum measurable length of the HOF. Recently, frequency-domain DMD measurement methods based on conventional interferometry setups, including optical frequency-domain interferometry (OFDR) and optical low coherence interferometry (OLCR), achieving higher measurement resolution, have been reported for short optical fiber sections [69], [70]. However, because of the short coherence length of the tunable laser (for OFDR) or the short moving length of the optical delay line (for OLCR), these previous interferometric techniques are also limited in regards to the maximum measurable length. In addition, the performance of measurements based on low-speed interferometry is significantly affected by the instability of the interferometer caused by environmental perturbations such as vibration, temperature fluctuation, and so on. The proposed ultrafast TS-OFDR technique is a very attractive solution for high-resolution and high-accuracy mode delay profile characterization of HOFs [51]. This tech-

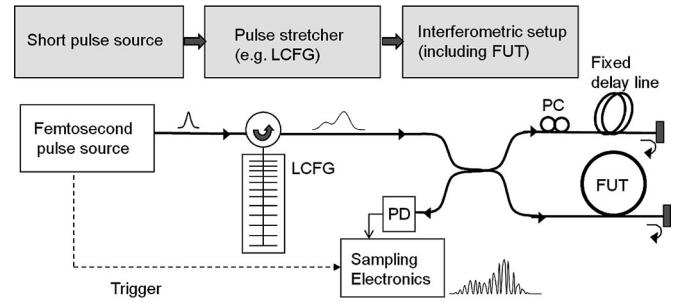


Fig. 6. Schematic concept diagram of the TS-OFDR-based modal delay measurements of an HOF as fiber under test (FUT); PC: polarization controller, PD: photodetector.

nique offers a resolution similar to conventional interferometric methods while allowing the characterization of much longer fiber sections (in fact, TS-OFDR based on pulse operation can be easily modified to carry our conventional time-of-flight measurement, thus extending the operation range of the instrument).

Fig. 6 shows a concept diagram of the TS-OFDR – based modal delay measurement for HOFs. A femtosecond fiber laser is commonly used. The temporally stretched pulses by a first-order dispersive element (e.g., LCFG) are launched into a fiber interferometer used to produce time-domain interference between the stretched optical pulses from the HOF sample (placed in one arm of the fiber interferometer) and the reference arm. Note that the LCFG can be located either at the input or at the output of the interferometer. The resultant temporal interferogram is acquired by fast photodetection followed by high-speed electronics. A conventional DFT-based numerical algorithm [7] is then used to obtain the modal delay profile of the multi-mode fiber under test. Note that as detailed above in Section II-B, the precise time-to-frequency map to be used in subsequent modal delay measurements can be simply obtained from a precalibration single interference pattern measurement.

In the experiment reviewed here [51], a short (5-m long) section of a HOF sample provided by OFS Labs. was accurately characterized. The femtosecond fiber laser (Pritel, Inc.) had a FWHM spectral BW of ~ 8 nm at a center wavelength of ~ 1553 nm and a repetition rate of 20 MHz. The LCFG used as a pulse stretcher was a 10-m long grating (Proximion, Inc.) with a first-order dispersion of 2000 ps/nm and a reflection BW of 42 nm. The light (~ 1.9 mW) was launched into the reference arm, which consisted of a fixed delay line (single-mode fiber, SMF, with nearly the same length as the sample fiber) to allow minimizing the dispersion mismatching between the two arms of the interferometer. The other light (~ 296 μ W) was launched into a 5 m section of the sample HOF under test. Fig. 7(a) shows the mode delay profile of the 5 m-long HOF measured by the proposed TS-OFDR technique. The reference arm consisted of a fixed delay line (single-mode fiber, SMF, with nearly the same length as the sample fiber) to achieve nearly the same time delay for the propagating pulses through the two arms of the interferometer (see Fig. 6). Many peaks induced by the internal and external interferences [71] in the HOF are generally observed in the mode-delay profile. The modal delay presented in

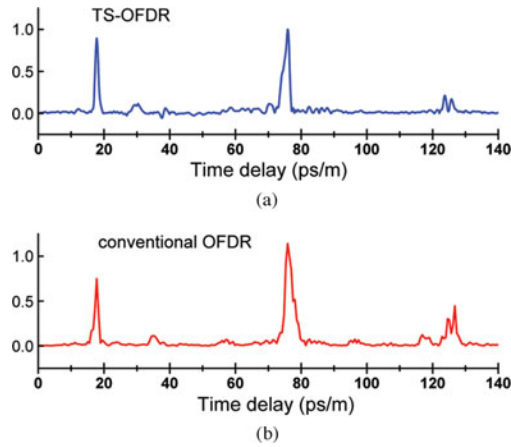


Fig. 7. (a) Modal delay profile of the HOF (5 m) measured by the proposed TS-OFDR technique; (b) conventional OFDR modal delay measurement based on CW tunable laser (from [51]).

Fig. 7(a) can be obtained by subtracting the modal delay originated by only internal interference among the excited modes in the HOF from the measured modal delay profile including both the internal and external interferences [51]. To confirm the peak distances obtained by our method, we also measured the modal delay using a conventional OFDR technique with a tunable CW laser, covering a wavelength range of 1540–1560 nm (same as that used in our TS-OFDR measurement, leading to a similar time resolution) with a sweeping speed of 5 nm/sec, see results in Fig. 7(b). The obtained curve by conventional means is very consistent with the modal delay profile obtained by the proposed TS-OFDR technique: We confirmed that there were four different excited modes in the HOF and that the last two peaks were very close, with a very good agreement between the time-delay values obtained from the two different measurement techniques.

The LCFG-induced linear frequency tuning rate of the stretched pulse is about 10^8 times faster than that achieved in the previously reported modal delay measurement of an HOF based on the use of a conventional OFDR technique with an external cavity tunable laser [69]–[71]. Thus, as compared with the conventional OFDR method, the proposed technique provides a much faster measurement speed, which translates into a significantly improved robustness against environmental perturbations such as the vibration of the fiber sample and/or temperature fluctuations. Moreover, the TS-OFDR setup can be also easily modified to implement the conventional time-domain technique [68], which is ideally suited for measuring much longer sections of the HOF under test. The proposed method should also prove useful for differential mode delay measurement of commercial multimode fibers in optical communications.

C. Real-Time Complex-Field Temporal Response Measurements of High-Speed Modulators

Temporal optical modulators, such as EO modulators and electro-absorption modulators, are commonly used in optical telecommunications [60]. Characterization of the phase and amplitude response of optical modulators to external drives is

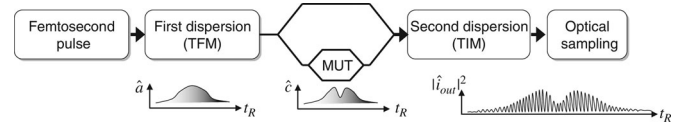


Fig. 8. Schematic diagram of the optical processing for the complex modulation characterization; TFM: time-to-frequency mapping; MUT: modulation-under-test; TIM: temporal-image magnification.

an essential procedure for diagnosing, controlling and optimizing the signal transmission performance in high-speed optical communication systems [72]–[74]. Most of the previously reported techniques allow only for an indirect characterization of the transmission response of the temporal modulator under test [72].

Recently, we have demonstrated a simple characterization technique based on a variant of TS-OFDR [52], [53], which enables direct detection of the complex (amplitude and phase) time-domain response of a high-speed optical modulator. The proposed approach is based on stretched pulse interference and allows one to characterize the modulation complex fields via measurements in either the time domain or the frequency domain. In particular, we have demonstrated direct and real-time diagnosis of the temporal impulse response of an EO modulator with a BW higher than 40 GHz, exceeding the photoreceiver BW in the measurement system. For this purpose, we have employed an advanced strategy in the chirped pulse interference system, referred to as “*common-path temporal-image-magnification process*,” which only requires the insertion of a second highly dispersive element in the measurement setup.

A schematic of the operation principle is shown in Fig. 8. Temporal stretching of an ultrashort pulse (e.g., induced by linear dispersion in a LCFG) is considered as a probe source to be modulated by the modulator-under-test. Use of the probe enables us to grab ultrafast complex temporal events (modulation) along the stretched pulse duration in the time and spectral domains [52], taking advantage of the time-frequency mapping induced by the linearly chirped pulse modulation process [75]. In particular, the modulated temporal waveform, $\hat{c}(t_R)$ can be written as [52], $\hat{c}(t_R) = \hat{a}(t_R) \cdot \hat{s}(t_R)$, where $\hat{s}(t_R)$ is the complex modulation (to be characterized) and $\hat{a}(t_R)$ is the time stretched (linearly chirped) pulse waveform, which is proportional to the input spectrum, \hat{A}_0 , with a proper frequency-to-time scaling, $\omega' = t_R / \Phi^{\text{first}}$. In addition, the spectrum of the modulated waveform is also proportional to the stretched pulse temporal profile with a time-to-frequency mapping defined by the same scaling factor, i.e., $\hat{C}(\omega') \propto \hat{A}_0(\omega') \hat{s}(t_R)$. Hence, the amplitude and the phase of the modulated waveform can be accurately reconstructed by applying stretched pulse interference (time-domain method) [52] or the conventional spectral interference technique (OFDR).

This original schematic exhibits a relatively severe limitation concerning the modulation BW that can be accurately characterized limited either by the photodetector BW or by the resolution of the spectral measurement. In our most recent work, this limitation has been overcome using a second pulse-stretching element (highly dispersive LCFG, Φ^{second})

after the modulation process (see Fig. 8), leading to an effective undistorted time-domain magnification of the temporal interference pattern [37]. In this case, the modulation time features are temporally stretched (with no additional distortion) following propagation through the second dispersive element by a factor of [53]

$$M = (\ddot{\Phi}^{\text{second}} + \ddot{\Phi}^{\text{first}}) / \ddot{\Phi}^{\text{first}}. \quad (14)$$

However, there is a restriction on the applied amount of GVD in the first stretcher, which should satisfy the following condition:

$$\Delta t \cdot \Delta t_s / 2\pi < |\ddot{\Phi}^{\text{first}}| \ll 8\pi / \Delta\omega_s^2 \quad (15)$$

where Δt is an estimate of the full time-width of the ultrashort input pulse, Δt_s is the duration of the complex modulation, and $\Delta\omega_s$ is the modulation BW. The lower boundary should be satisfied in order to avoid any truncation of the complex modulation when modulating on the chirped pulse in the second processing stage (see Fig. 8). The upper boundary, which is more restrictive as it depends on the square of the modulation BW, ensures that the temporal complex modulation is accurately transferred into the spectral domain (TFM) without loss of information [75]. A similar temporal-image-magnification technique has been reported for increasing the effective BW of high-speed ADC [37]. It is important to mention that our method allows undistorted time stretching and subsequent recovering of the *complex-field* information of the modulation, while previous methods for temporal stretching of modulation waveforms [37] were limited to operation on the signal amplitude profile.

As an application example of the proposed method [53], we tested a lithium niobate (z-cut) EO intensity modulator with EO BW ≥ 35 GHz (E-O Space, Inc.). An ultrashort pulse (FWHM BW ≈ 2.7 nm), generated from a femtosecond fiber laser (Pritel, Inc.) operating at a 16.7 MHz repetition rate and at an optical wavelength of ~ 1544 nm, was first temporally stretched by linear reflection in a 5-cm-long LCFG introducing a total dispersion of 170 ps/nm for the TFM. The stretched pulse with ≈ 431 -ps FWHM time duration was amplified and split by a 70/30 fiber coupler. The optical modulator under test was located in one of the coupler's arms. The other coupler's arm was used as the reference. The pulse average power in the reference arm was 33.3 μ W. The pulse average power at the output of the modulator was varied depending on the applied bias voltage (< 100 μ W). After combining the two signals through a 50/50 fiber coupler, the generated interferograms were temporally stretched with the second LCFG (2000 ps/nm, Proximion, Inc.) for common-path temporal-image magnification by a factor of 12.7 (= (2000+170)/170). This interference was acquired in the spectral domain using an OSA (resolution = 10 pm) and in the time domain using a sampling oscilloscope with an optical sampler of ≈ 20 GHz 3 dB- BW. The reconstructed amplitude and phase profiles by the spectral and the time domain methods are shown in Figs. 9 and 10, respectively. An input electric pulse with 28 ps at FWHM was used as the input excitation in the EO modulator; this pulse, shown in the inset of Fig. 2, was generated by simply converting the ultrashort optical pulse from the fiber laser into an electric signal using a high-speed photodiode.

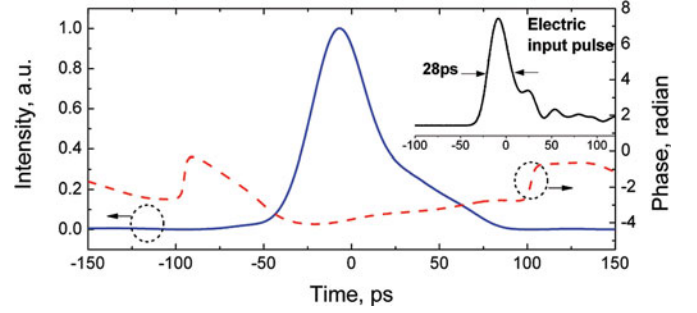


Fig. 9. Spectral-domain detection: temporal amplitude and phase responses of the intensity modulator to the 28 ps FWHM electric pulse (inset) (from [53]).

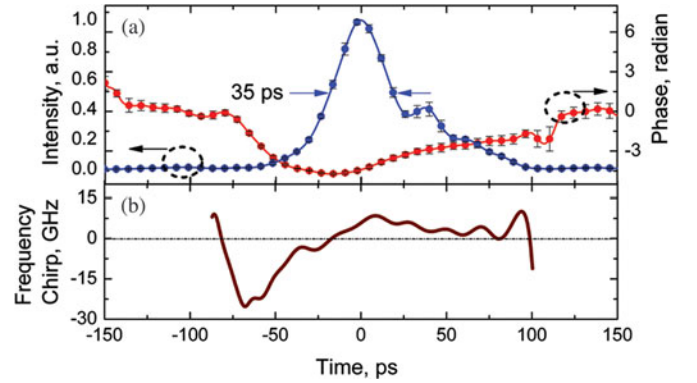


Fig. 10. Time-domain detection: (a) temporal amplitude and phase responses for the same modulation and (b) corresponding frequency chirp (from [53]).

There was a very good agreement between the results obtained from time-domain and spectral-domain measurements. However, more detailed features could be observed from the time domain method (see Fig. 10) compared to the spectral domain approach (see Fig. 9), which clearly evidenced the effectiveness of the proposed LCFG-induced temporal-image-magnification procedure for increasing the measurable modulation BW. Complex time responses with features as fast as ≈ 35 ps (FWHM) were successfully characterized. Measurement accuracy is also shown in terms of the standard deviation for five consecutive reconstructions of the amplitude and the phase profiles; see error bars in Fig. 10(a). Finally, the instantaneous frequency chirp [see Fig. 10(b)] was numerically derived from the reconstructed phase profile.

A key advantage of implementing the complex modulation characterization in the time domain is that one can monitor the dynamics of the complex modulation not only in a direct fashion but also in *real time* owing to the fast acquisition feature. An example of this critical capability of our method has been also demonstrated [53] by successfully monitoring a pulse modulation process as the bias voltage was rapidly tuned in a Mach-Zehnder EO modulator. Full field information (amplitude and phase) of the modulation signal has been obtained at 30 frames per second, with a time magnification factor of 21.

IV. REAL-TIME OCT BIOMEDICAL IMAGING BY TS-OFDR

In recent years, wavelength swept-source OCT (SS-OCT) technologies based on standard OFDR [17]–[19], [21]–[23], [25]–[27] have demonstrated greatly advantageous for *in vivo* biological imaging, especially in ophthalmology, providing an unparalleled performance in terms of image acquisition rate and sensitivity. This superiority has been recently emphasized with experimental observations of motion artifacts shown in *in vivo* OCT images [76]. As discussed in Section I, the recently introduced TS-OFDR technique [30]–[34] offers the potential to reach image acquisition speeds with A-line rates up to a few tens of megahertz, similar or higher than state-of-the-art SS-OCT methods using a far simpler scheme, e.g., all-passive wavelength sweeping. However, the reported performance of pioneering TS-OFDR systems could not reach the level that is required for biological OCT imaging mainly due to the poor reflectivity sensitivity, ranged from -40 dB [30] to -60 dB [31]. In a recent work, the sensitivity of a TS-OFDR system has been further improved up to -68 dB by the use of a digital normalization detection technique [56]. An ultrafast OCT scheme based on TS-OFDR consisting of a supercontinuum source with a 350 nm BW at 1550 nm center wavelength and a dispersive optical fiber as a pulse-stretching element has been reported [30]. A 20-km commercial dispersion-shifted fiber was used to stretch the supercontinuum pulse. The zero-dispersion wavelength (ZDW) of the DSF was 1547 nm and the dispersion slope at the ZDW was 0.066 ps/nm².km. In this demonstration, a 5-MHz axial-line scanning rate and a 8 - μ m axial resolution were achieved. The sensitivity of this fiber-based TS-OFDR was about -40 dB, while the shot-noise level of the used photodetection system was about -60 dB. This difference of 20 dB was thought to come from the intensity noise of the supercontinuum source. Because of this poor sensitivity, the system was not able to provide an image of a biological sample with a reasonable quality. Instead, a piece of lint-free cleaning tissue was used as a sample for 2-D-OCT imaging due to its relatively strong reflection combined with a micron-scale structure. To effectively suppress the effect of RIN in the OCT scheme to enhance the sensitivity and dynamic range, the same research group has recently introduced a digital normalization detection technique which removes both the additive and convolutional contributions of the RINs in the final interferogram signals by numerically manipulating the temporal signal of the input swept source and two different π -phase shifted temporal interferograms [56]. This technique, which is similar to a numerical dual-balanced detection scheme, achieved -68 dB sensitivity in the ultrafast OCT system, still insufficient for biological sample imaging. In this section, we demonstrate biological OCT imaging based on TS-OFDR using a highly dispersive LCFG. For this demonstration [54], an improved sensitivity of -82 dB was achieved using a high-speed (3-GHz BW) balanced photodetector. The axial resolution of this OCT system was also improved with respect to our first demonstrated TS-OFDR setup [31] up to ~ 42 μ m by utilizing the full-reflection BW (45 nm) of the used LCFG. In our experimental demonstration, a 2-D OCT image of an onion sample has been obtained with a 5 MHz

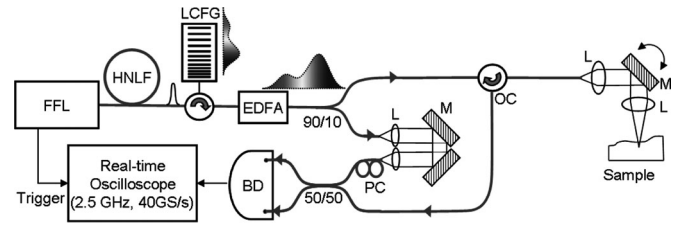


Fig. 11. Schematic of real-time OCT setup based on TS-OFDR. Femtosecond fiber laser (FFL), highly nonlinear fiber (HNLf), linearly chirped fiber Bragg grating (LCFG), erbium-doped fiber amplifier (EDFA), optical circulator (OC), optical collimator (L), mirror (M), polarization controller (PC), and balanced detector (BD).

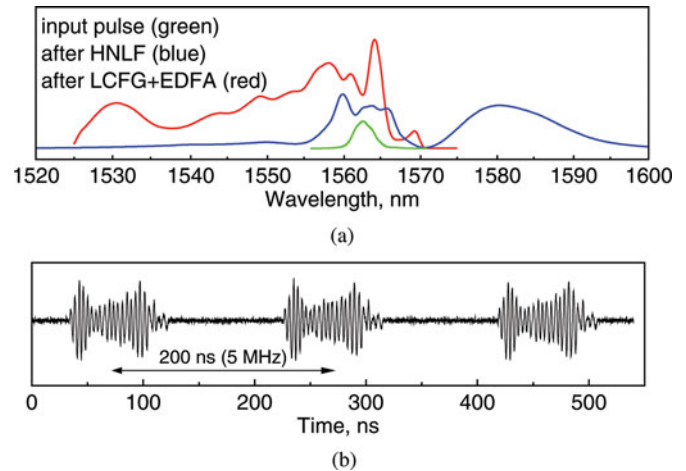


Fig. 12. (a) Pulse spectra: input spectrum of femtosecond pulse laser (green curve), SPM-broadened pulse spectrum (blue curve), and spectrally filtered and amplified spectrum of the stretched pulse (red curve); (b) 5 MHz repetition rate temporal interferograms acquired through balanced detection.

A-line rate over a total measurement time of ~ 173 μ s for a 0.66 mm transverse scan. These experiments clearly prove the very strong potential of TS-OFDR for ultrahigh-speed, high-quality *in vivo* biomedical imaging, particularly considering that further resolution and sensitivity improvements are readily feasible.

Fig. 11 shows a schematic of the setup used for real-time OCT based on TS-OFDR. The input pulse in our experiments was a nearly transform-limited Gaussian pulse spectrally centered at 1562.7 nm and with a time-width/ BW of 1.1 ps/3 nm (FWHM) [see green curve in Fig. 12(a)], which was directly generated from a passively mode-locked fiber laser (Pritel, Inc) operating at a repetition rate of 5 MHz. The input pulse probe was launched into a nonlinear fiber (Pulse Compressor, Pritel, Inc.) in order to induce a spectral broadening by super-continuum generation; a 70-nm pulse BW was obtained at the nonlinear fiber output by properly adjusting the input pulse peak power, see blue curve in Fig. 12(a). The pulse BW was finally filtered to ≈ 36.4 nm (FWHM) [see red curve in Fig. 12(a)] by linear reflection in a 10-m-long LCFG (+2000-ps/nm dispersion, 42 nm (3 dB BW), from Proximion, Inc.), which resulted in optical pulses each with a duration of 80 ns and repeating at 5 MHz; these pulses were subsequently amplified with an erbium-doped fiber amplifier (EDFA). The average power of the

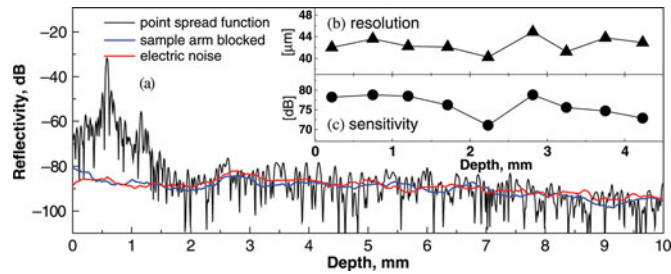


Fig. 13. (a) Depth profile of a single-reflection sample (black curve), depth profile when the sample arm was blocked (blue curve), and electrical amplifier noise (red curve), (b) resolutions, and (c) sensitivities with respect to axial depth.

amplified pulse was measured to be ~ 3 mW. The relative time delay between the two arms in the setup was adjusted using the installed mirror (M) in order to ensure that the two pulses from each arm were properly delayed with respect to each other so that to generate the desired interferogram over a time period of the stretched pulse. A 1-D scanning probe with a galvanometer driver (dynAXIS, ScanLab, Inc.) was used for scanning the probe beam along the transversal direction. The A-lines were acquired by a real-time oscilloscope with a 2.5-GHz BW and a maximum 40-GS/s sample rate (Tektronix DPO7254). Interference signals [see Fig. 12(b)] were acquired by a high-speed (3 dB BW of 2.8 GHz) balanced detector (MFA optics, Inc.) for which the common-mode rejection ratio (CMRR) was tested to be over 30 dB up to 2 GHz. Fig. 12(b) confirms that each individual stretched pulse (single interferogram) did not overlap with neighbouring pulses and that the “dc” component of the interferogram was decoupled by the balanced detection.

The axial resolution was estimated to be $42 \mu\text{m}$, which agrees well with the transform-limited theoretical resolution of $43 \mu\text{m}$ calculated from (12) above. For a single low-reflection sample with a reflectivity of -31.6 dB, the reconstructed axial-reflectivity profile in logarithmic scale is shown in Fig. 13(a) (black line). The maximum achievable sensitivity in our experiment was determined to be ≈ -82 dB from Fig. 13(a). This sensitivity level is unprecedented for TS-OFDR [30]–[34], and it was achieved by: 1) employing balanced photodetection, and 2) applying the HTCMT on the measured interferograms to suppress the nonlinear phase errors mainly induced by the LCFG and the spectral broadening of the input pulse (see descriptions in Section II-B). The performance uniformity of our OCT system, in terms of resolution and sensitivity, was tested by axially displacing the single-point reflection sample with a 0.5 mm moving step up to a total depth range of 4.5 mm (corresponding to a 7 dB sensitivity reduction) [see results in Fig. 13(b) and (c)]. Overall, our OCT imaging system exhibited a fairly uniform performance over the tested depth range: The resolution was ranged from 41.2 to $44.9 \mu\text{m}$ and the sensitivity varied from -71.1 to -78.8 dB. This was, in part, enabled by the predominantly linear group delay introduced by the dispersive LCFG over the entire operational spectral BW.

For the 2-D OCT imaging demonstration, we acquired 864 A-lines of the temporal interferograms repeating at 5 MHz within a total time window of $173 \mu\text{s}$ by using the real-time oscilloscope set to a sample rate of 5 GS/s and 865 K total data

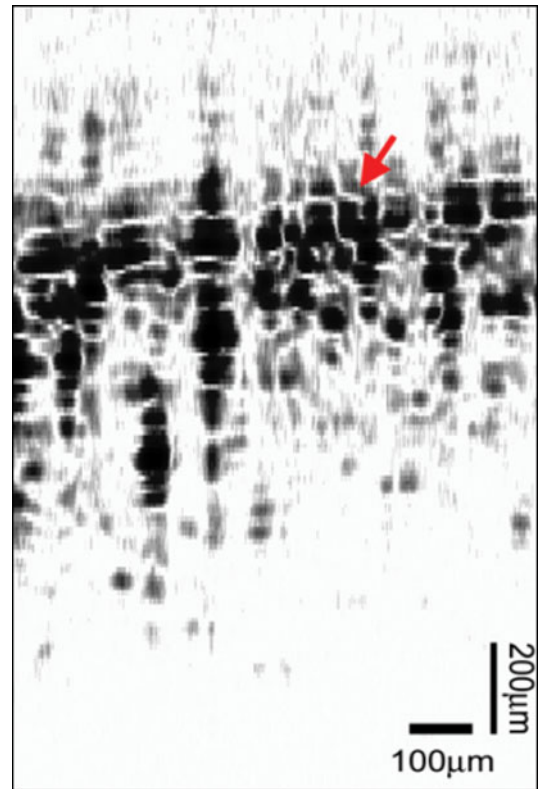


Fig. 14. OCT image of an onion sample (logarithmic scale, 190×432 pixels, 2 mm depth \times 0.66 mm width).

points for each acquired temporal interferogram. We note that due to the limited frame rate of the available oscilloscope, all the A-lines required for reconstruction of a 2-D image were acquired in a single frame. In the signal processing stage, temporal interferograms along the time duration (~ 80 ns) of the stretched pulse were consecutively selected to generate the corresponding A-line depth profiles by referring to the associated triggering signals. Fig. 14 shows a tomographic image (2 mm depth \times 0.66 mm width) of an onion sample using a logarithmic inverse gray scale. The Galvo mirror was scanned at 600 Hz, which is obviously very low scan speed in comparison with our A-line scan rate. Fig. 14 shows a down-sampled image for which only one of every two consecutive recorded A-lines was used for constructing the OCT image; note that the full set of A-lines did not show any more detailed information than the presented interlaced A-lines set. Fig. 14 shows that the achieved axial resolution of $\sim 42 \mu\text{m}$ was clearly sufficient to resolve the cell layers of the analyzed onion sample. Note that the axial resolution can be improved by broadening the pulse spectrum, using a short wavelength band (e.g., 1310 or 850 nm) pulse, and/or redesigning the LCFG to have a wider reflection BW. As evidenced by the results shown in Fig. 13, the sensitivity in our demonstrator was limited by electrical amplifier noise in the high-speed photodetector, and thus, the shot-noise detection limit was not reached. Balanced detection keeps improving in terms of speed (> 10 GHz) and noise suppression ratio. The sensitivity of the proposed TS-OFDR technique could thus be further improved by use of an optimized balanced detection scheme and very stable ultrafast pulsed lasers. The total number

of A-lines to be acquired in real time may be limited at full depth ranging due to the large number of sampling points per A-line (~ 4000 points-per-line at 40 GS/s) and limited onboard memory size (< 2 GB). One may compromise the depth range in order to increase the number of lines to be acquired in real time for 2-D imaging.

The proof-of-concept OCT experiments reported here were carried out in the telecommunication wavelength region around $1.5 \mu\text{m}$. It is well known that this light wavelength region suffers from strong water absorption, and thus, operation at other wavelength bands may be preferred for biomedical tissue imaging, e.g., around 800 nm [4]. Obviously, the reported TS-OFDR scheme for OCT imaging can be also implemented over this more conventional wavelength region since all the needed components are also available in the 800-nm band. Concerning the dispersive medium, fiber Bragg gratings can be designed and fabricated for operation around 800 nm [58], but presently, fiber grating technology is more widely available for operation at the low-loss telecommunication wavelength band around $1.5 \mu\text{m}$. Dispersive optical fibers are readily available for their use over a very broad range of wavelength regions, including the 800-nm band, and as a result, they represent an interesting alternative to introduce the needed dispersion in a 800-nm TS-OFDR system.

V. CONCLUSION

This paper has reviewed recent progress on a new technique for ultrahigh-speed OFDR, namely, TS-OFDR. This method is essentially based on the use of linear GVD-induced frequency-to-time mapping of the target broadband spectral interferogram so that this information can be captured in *real time* using a single photodetection stage (single-ended or balanced photoreceiver) and a fast ADC. Advantages of TS-OFDR include: 1) its capability of achieving ultrarapid axial line acquisition rates, as high as the pulse repetition rate from the seeded optical source (up to a few tens of megahertz), 2) the simple all-passive nature of the wavelength sweeping mechanism (linear dispersion), and 3) the possibility of adapting the scheme for conventional time-of-flight measurements, providing a complementary set of performance specifications. Some applications exploiting the unique features of TS-OFDR have been also reviewed, including: 1) real-time monitoring of group-delay characteristics of fiber-optics components, 2) highly accurate modal-delay measurements in high-order mode optical fibers, and 3) real-time complex-field temporal response characterization of optical modulators with BWs in the tens-of-gigahertz range.

We have shown that a megahertz-update rate TS-OFDR system can be configured to achieve the performance that is required for micrometer-resolution imaging over depth ranges up to a few centimeters, thus being promising for biomedical-imaging applications (OCT). A main limitation of TS-OFDR is its relatively poor sensitivity, which is, in part, due to the intrinsic signal peak power loss associated with any dispersive process. Still, 2-D imaging of biological tissue with a resolution of $\sim 40 \mu\text{m}$ and a sensitivity above -80 dB, captured at a 5-MHz axial-line rate, has been reported here. In our system demonstrator, the resolution and sensitivity were limited by the spectral

BW of the LCFG and the electrical amplifier noise of the used high-speed balanced detector, respectively. Thus, considering that improvements of these two critical performance specifications are readily feasible, the potential of TS-OFDR for advanced imaging applications, including OCT, appear to be very strong.

We believe that the TS-OFDR technology should also prove useful for other traditional applications of OFDR, e.g., sensing, ranging, material analysis etc., offering all the discussed key performance advantages. In principle, TS-OFDR requires the use of a coherent (ultrashort pulse) light source, e.g., mode-locked laser. However, recent studies have demonstrated the possibility of using incoherent light for GVD-induced time-domain spectral interferometry [77], [78]. To give a relevant example, a similar schematic to that described in Section III-A for group-delay characterization of dispersive devices has been recently proposed using broadband incoherent light [77]. This concept has been recently extended and applied for group-delay characterization of fiber-optics dispersion elements over BWs exceeding 40 nm (entire C band) at a video update rate [78]. The use of incoherent light instead of mode-locked lasers translates into important practical advantages, including the possibility of reaching extremely broad frequency BWs in a relatively simpler and less costly fashion. All these recent advances clearly point out the promising potential of TS-OFDR for a large number of unexplored applications using either coherent or incoherent broadband light sources.

APPENDIX I

Using the definitions introduced above in Section II-A, the envelope of the temporal impulse response that characterizes linear propagation through a first-order dispersive medium is [36]

$$\hat{h}(t_R) \propto \exp\left(j\frac{1}{2\Phi}t_R^2\right) \quad (\text{A1})$$

where \propto means proportional, $t_R = t - \dot{\Phi}$, $\dot{\Phi}$ is the medium's group delay (around the carrier radial frequency ω_0 of the propagating optical signal), and $\ddot{\Phi}$ is the medium's first-order dispersion coefficient (GVD). The time envelope of the input signal launched into the dispersive filter is defined as $\hat{a}_1(t_R)$. This signal is assumed to be time limited with a total time duration (full time width) defined by Δt_1 . The optical signal at the output of this filter is spectrally centered at the same carrier frequency, ω_0 , and it has a time envelope defined by the following convolution integral:

$$\begin{aligned} \hat{a}_2(t_R) &= \hat{a}_1(t_R) * \hat{h}(t_R) = \int_{-\infty}^{+\infty} d\tau \hat{a}_1(\tau) \hat{h}(t_R - \tau) \\ &= \int_{-\Delta t_1/2}^{+\Delta t_1/2} d\tau \hat{a}_1(\tau) \hat{h}(t_R - \tau). \end{aligned} \quad (\text{A2})$$

Introducing the expression for $\hat{h}(t_R)$ is (A1.1) into the convolution integral in (A1.2), we obtain

$$\hat{a}_2(t_R) \propto \int_{-\Delta t_1/2}^{+\Delta t_1/2} d\tau \hat{a}_1(\tau) \exp\left(j\frac{1}{2\Phi}[t_R - \tau]^2\right)$$

TABLE I
 SOME HTS

$f(x)$	$F_{HT}(x)$
$\cos(x)$	$-\sin(x)$
$\sin(x)$	$\cos(x)$
$\frac{\sin(x)}{x}$	$\frac{\cos(x)-1}{x}$
$\delta(x)$	$-\frac{1}{\pi x}$

$$\begin{aligned}
 &= \exp\left(j\frac{1}{2\ddot{\Phi}}t_R^2\right) \int_{-\Delta t_1/2}^{+\Delta t_1/2} d\tau \hat{a}_1(\tau) \\
 &\quad \times \exp\left(j\frac{1}{2\ddot{\Phi}}\tau^2\right) \exp\left(-j\frac{1}{\ddot{\Phi}}t_R\tau\right). \quad (\text{A3})
 \end{aligned}$$

Considering that the integral in (AI.3) extends from $\tau = -\Delta t_1/2$ to $\tau = +\Delta t_1/2$, the factor $\exp\left(j\tau^2/2\ddot{\Phi}\right)$ within the integral can be neglected if the following condition is satisfied:

$$\left| \frac{\Delta t_1^2}{8\ddot{\Phi}} \right| \ll \pi. \quad (\text{A4})$$

In this case, the quadratic phase factor is negligible over the whole range of the integral. Equation (AI.4) is usually referred to as the temporal Fraunhofer condition [36]. Under this condition, (AI.3) can be approximated by a Fourier integral of the input signal envelope:

$$\begin{aligned}
 \hat{a}_2(t_R) &\propto \exp\left(j\frac{1}{2\ddot{\Phi}}t_R^2\right) \int_{-\Delta t_1/2}^{+\Delta t_1/2} d\tau \hat{a}_1(\tau) \exp\left(-j\frac{1}{\ddot{\Phi}}t_R\tau\right) \\
 &= \exp\left(j\frac{1}{2\ddot{\Phi}}t_R^2\right) \int_{-\Delta t_1/2}^{+\Delta t_1/2} d\tau \hat{a}_1(\tau) \exp(-j\omega'\tau)
 \end{aligned} \quad (\text{A5})$$

with $\omega' = t_R/\ddot{\Phi}$. (AI.5) is more typically expressed as follows:

$$\hat{a}_2(t_R) \propto \exp\left(j\frac{1}{2\ddot{\Phi}}t_R^2\right) \left\{ \hat{A}_1(\omega') \right\}_{\omega'=t_R/\ddot{\Phi}} \quad (\text{A6})$$

where $\hat{A}_1(\omega')$ is the Fourier transform of $\hat{a}_1(t_R)$, $\hat{A}_1(\omega') = \mathfrak{F}\{\hat{a}_1(t_R)\}$. This is the so-called temporal Fraunhofer approximation in the problem of linear propagation of a time-limited optical waveform through a first-order dispersive medium.

APPENDIX II

The HT of $f(x)$ is defined by [79]

$$F_{HT}(x) = \frac{1}{\pi} \int_{-\infty}^{\infty} \frac{f(x')dx'}{x' - x} = \frac{-1}{\pi x} * f(x). \quad (\text{A7})$$

The divergence at $x = x'$ allowed for by taking the Cauchy principal value of the integral. It will be seen that $F_{HT}(x)$ is a linear functional of $f(x)$; in fact it is obtainable from $f(x)$ by convolution with $(\pi x)^{-1}$. From the convolution theorem we can

now say how the spectrum of $F_{HT}(x)$ is related to that of $f(x)$. The Fourier transformation of $(-\pi x)^{-1}$ is $i \operatorname{sgn} s$, which is equal to $+i$ for positive s and $-i$ for negative s ; hence, HT is equivalent to a specific kind of filtering, in which the amplitudes of the spectral components are left unchanged, but their phases are altered by $\pi/2$, positively or negatively according to the sign of s . Note that all cosine components transform into negative sine components and that all sine components transform into cosines. A consequence of this is that the HTs of even functions are odd and those of odd functions are even.

ACKNOWLEDGMENT

The authors would like to thank the following individuals for important contributions to some of the works reviewed here: Dr. J. C. Kieffer (INRS-EMT), Dr. D. J. Moss (University of Sydney), and Dr. S. Ramachandran (Boston University, formerly at OFS Labs). Authors also express their gratitude to the anonymous referees and Prof. A. Weiner for their very useful and relevant comments on their paper, which have greatly helped them to improve the quality of the paper.

REFERENCES

- [1] R. C. Youngquist, S. Carr, and D. E. N. Davies, "Optical coherence-domain reflectometry: a new optical evaluation technique," *Opt. Lett.*, vol. 12, pp. 158–160, 1987.
- [2] K. Takada, I. Yokohama, K. Chida, and J. Noda, "New measurement system for fault location in optical waveguide devices based on an interferometric technique," *Appl. Opt.*, vol. 26, pp. 1603–1606, 1987.
- [3] B. L. Danielson and C. D. Whittenberg, "Guided wave reflectometry with micrometer resolution," *Appl. Opt.*, vol. 26, pp. 2836–2842, 1987.
- [4] D. Huang, E. A. Swanson, C. P. Lin, J. S. Schuman, W. G. Stinson, W. Chang, M. R. Hee, T. Flotte, K. Gregory, C. A. Puliafito *et al.*, "Optical coherence tomography," *Science*, vol. 254, pp. 1178–1181, 1991.
- [5] W. Eickhoff and R. Ulrich, "Optical frequency domain reflectometry in single-mode fiber," *Appl. Phys. Lett.*, vol. 39, pp. 693–695, 1981.
- [6] H. Barfu and E. Brinkmeyer, "Modified optical frequency domain reflectometry with high spatial resolution," *J. Lightw. Technol.*, vol. 7, pp. 3–10, 1989.
- [7] U. Glombitza and E. Brinkmeyer, "Coherent frequency-domain reflectometry for characterization of single-mode integrated-optical waveguides," *J. Lightw. Technol.*, vol. 11, pp. 1377–1384, 1993.
- [8] R. Passy, N. Gisin, J. P. von der Weid, and H. H. Gilgen, "Experimental and theoretical investigations of coherent OFDR with semiconductor laser sources," *J. Lightw. Technol.*, vol. 12, pp. 1622–1630, 1994.
- [9] J. P. von der Weid, R. Passy, G. Mussi, and N. Gisin, "On the characterization of optical fiber network components with optical frequency domain reflectometry," *J. Lightw. Technol.*, vol. 15, pp. 1131–1141, 1994.
- [10] A. F. Fercher, C. K. Hitzenberger, G. Kamp, and S. Y. El-Zaiat, "Measurement of intraocular distances by backscattering spectral interferometry," *Opt. Comms.*, vol. 117, pp. 43–48, 1995.
- [11] B. Golubovic, B. E. Bouma, G. J. Tearney, and J. G. Fujimoto, "Optical frequency-domain reflectometry using rapid wavelength tuning of a Cr4+:forsterite laser," *Opt. Lett.*, vol. 22, pp. 1704–1706, 1997.
- [12] D. K. Gifford, B. J. Soller, M. S. Wolfe, and M. E. Froggatt, "Optical vector network analyzer for single-scan measurements of loss, group delay, and polarization mode dispersion," *Appl. Opt.*, vol. 44, pp. 7282–7286, 2005.
- [13] B. Soller, D. Gifford, M. Wolfe, and M. Froggatt, "High resolution optical frequency domain reflectometry for characterization of components and assemblies," *Opt. Exp.*, vol. 13, pp. 666–674, 2005.
- [14] I. Coddington, W. C. Swann, L. Nenadovic, and N. R. Newbury, "Rapid and precise absolute distance measurements at long range," *Nat. Phot.*, vol. 3, pp. 351–356, 2009.
- [15] B. E. Bouma and G. J. Tearney, *Handbook of Optical Coherence Tomography*. New York: Marcel Dekker, 2002.
- [16] D. Uttam and B. Culshaw, "Precision time domain reflectometry in optical fiber systems using a frequency modulated continuous wave ranging

- technique," *IEEE J. Lightw. Technol.*, vol. 3, no. 5, pp. 971–977, Oct. 1985.
- [17] R. Leitgeb, C. K. Hitzenberger, and A. F. Fercher, "Performance of Fourier domain vs. time domain optical coherence tomography," *Opt. Exp.*, vol. 11, pp. 889–1894, 2003.
- [18] J. F. de Boer, B. Cense, B. H. Park, M. C. Pierce, G. J. Tearney, and B. E. Bouma, "Improved signal-to-noise ratio in spectral-domain compared with time-domain optical coherence tomography," *Opt. Lett.*, vol. 28, pp. 2067–2069, 2003.
- [19] M. A. Choma, M. V. Sarunic, C. Y. Yang, and J. A. Izatt, "Sensitivity advantage of swept source and Fourier domain optical coherence tomography," *Opt. Exp.*, vol. 11, pp. 2183–2189, 2003.
- [20] K. Takada, H. Yamada, Y. Hibino, and S. Mitachi, "Range extension in optical low coherence reflectometry achieved by using a pair of retroreflectors," *Electron. Lett.*, vol. 31, pp. 1565–1567, 1995.
- [21] S. H. Yun, G. J. Tearney, J. F. de Boer, N. Iftima, and B. E. Bouma, "High-speed optical frequency-domain imaging," *Opt. Exp.*, vol. 11, pp. 2953–2963, 2003.
- [22] S. H. Yun, G. J. Tearney, J. F. de Boer, and B. E. Bouma, "Motion artefacts in optical coherence tomography with frequency-domain ranging," *Opt. Exp.*, vol. 12, pp. 2977–2998, 2004.
- [23] M. Sumetsky, N. M. Litchinitser, P. S. Westbrook, and Y. Li, "Group delay ripple in chirped fiber Bragg gratings: theory, measurement, and reduction," *Bragg Gratings, Photosensitivity, and Poling in Glass Waveguides, Tech. Dig.*, Monterey, CA, 2003, Paper MB1.
- [24] B. Potsaid, I. Gorczynska, V. J. Srinivasan, Y. Chen, J. Jiang, A. Cable, and J. G. Fujimoto, "Ultra-high speed spectral/Fourier domain OCT ophthalmic imaging at 70000 to 312500 axial scans per second," *Opt. Exp.*, vol. 16, pp. 15149–15169, 2008.
- [25] R. Huber, M. Wojtkowski, K. Taira, J. G. Fujimoto, and K. Hsu, "Amplified, frequency swept lasers for frequency domain reflectometry and OCT imaging: design and scaling principles," *Opt. Exp.*, vol. 13, pp. 3513–3528, 2005.
- [26] R. Huber, M. Wojtkowski, and J. G. Fujimoto, "Fourier Domain Mode Locking (FDML): A new laser operating regime and application for optical coherence tomography," *Opt. Exp.*, vol. 14, pp. 3225–3237, 2006.
- [27] R. Huber, D. C. Adler, and J. G. Fujimoto, "Buffered Fourier domain mode locking: unidirectional swept sources for optical coherence tomography imaging at 370000 lines/s," *Opt. Lett.*, vol. 31, pp. 2975–2977, 2006.
- [28] W. Wieser, B. R. Biedermann, T. Klein, C. M. Eigenwillig, and R. Huber, "Multi-Megahertz OCT: High quality 3D imaging at 20 million A-scans and 4.5 G Voxels per second," *Opt. Exp.*, vol. 18, pp. 14685–14704, 2010.
- [29] T.-J. Ahn, J. Y. Lee, and D. Y. Kim, "Suppression of nonlinear frequency sweep in an optical frequency-domain reflectometer by use of Hilbert transformation," *Appl. Opt.*, vol. 44, pp. 7630–7634, 2005.
- [30] S. Moon and D. Y. Kim, "Ultra-high-speed optical coherence tomography with a stretched pulse supercontinuum source," *Opt. Exp.*, vol. 14, pp. 11575–11584, 2006.
- [31] Y. Park, T.-J. Ahn, J.-C. Kieffer, and J. Azaña, "Optical frequency domain reflectometry based on real-time Fourier transformation," *Opt. Exp.*, vol. 15, pp. 4597–4616, 2007.
- [32] R. E. Saperstein, N. Alic, S. Zamec, K. Ikeda, B. Slutsky, and Y. Fainman, "Processing advantages of linear chirped fiber Bragg gratings in the time domain realization of optical frequency-domain reflectometry," *Opt. Exp.*, vol. 15, pp. 15464–15479, 2007.
- [33] K. Goda, D. R. Solli, and B. Jalali, "Real-time optical reflectometry enabled by amplified dispersive Fourier transformation," *Appl. Phys. Lett.*, vol. 93, pp. 031106-1–031106-3, 2008.
- [34] H. Xia and C. Zhang, "Ultrafast and Doppler-free femtosecond optical ranging based on dispersive frequency-modulated interferometry," *Opt. Exp.*, vol. 18, pp. 4118–4129, 2010.
- [35] Y. C. Tong, L. Y. Chan and H. K. Tsang, "Fibre dispersion or pulse spectrum measurement using a sampling oscilloscope," *Electron. Lett.*, vol. 33, pp. 983–1985, 1997.
- [36] J. Azaña and M. A. Muriel, "Real-time optical spectrum analysis based on the time-space duality in chirped fiber gratings," *IEEE J. Quantum Electron.*, vol. 36, no. 5, pp. 517–526, May 2000.
- [37] F. Coppinger, A. S. Bhushan, and B. Jalali, "Photonic time stretch and its application to analog-to-digital conversion," *IEEE Trans. Microwave Theory Tech.*, vol. 47, no. 7, pp. 1309–1314, Jul. 1999.
- [38] J. Chou, Y. Han, and B. Jalali, "Adaptive RF-photonic arbitrary waveform generator," *IEEE Photon. Technol. Lett.*, vol. 15, pp. 581–583, 2003.
- [39] J. Azaña, N. K. Berger, B. Levit, and B. Fischer, "Broadband arbitrary waveform generation based on microwave frequency upshifting in optical fibers," *J. Lightw. Technol.*, vol. 24, no. 7, pp. 2663–2675, Jul. 2006.
- [40] D. R. Solli, J. Chou, and B. Jalali, "Amplified wavelength-time transformation for real-time spectroscopy," *Nature Photon.*, vol. 2, pp. 48–51, 2008.
- [41] K. Goda, K. K. Tsia, and B. Jalali, "Serial time-encoded amplified imaging for real-time observation of fast dynamic phenomena," *Nature*, vol. 458, pp. 1145–1149, 2009.
- [42] R. M. Fortenberry, W. V. Sorin, H. Lin, and S. A. Newton, "Low-power ultrashort optical pulse characterization using linear dispersion," in *Proc. Conf. Opt. Fiber Commun.*, 1997, pp. 290–291.
- [43] C. Dorrer, "Chromatic dispersion characterization by direct instantaneous frequency measurement," *Opt. Lett.*, vol. 29, pp. 204–206, 2004.
- [44] N. K. Berger, B. Levit, V. Smulakovsky, and B. Fischer, "Complete characterization of optical pulses by real-time spectral interferometry," *Appl. Opt.*, vol. 44, pp. 7862–7866, 2005.
- [45] T. J. Ahn, Y. Park, and J. Azaña, "Improved optical pulse characterization based on feedback-controlled Hilbert transformation temporal interferometry," *IEEE Photon. Technol. Lett.*, vol. 20, no. 7, pp. 475–477, 2008.
- [46] M. H. Asghari, Y. Park, and J. Azaña, "Complex-field measurement of ultrafast dynamic optical events based on real-time spectral interferometry," *Opt. Exp.*, vol. 18, pp. 16526–16538, 2010.
- [47] J. Azaña, N. K. Berger, B. Levit, and B. Fischer, "Reconfigurable generation of high-repetition-rate optical pulse sequences based on time-domain phase-only filtering," *Opt. Lett.*, vol. 30, pp. 3228–3230, 2005.
- [48] R. E. Saperstein and Y. Fainman, "Information processing with longitudinal spectral decomposition of ultrafast pulses," *Appl. Opt.*, vol. 47, pp. A21–A31, 2008.
- [49] S. Thomas, A. Malacarne, F. Fresi, L. Potì, A. Bogoni, and J. Azaña, "Fiber-based programmable picosecond arbitrary optical pulse shaper," *J. Lightw. Technol.*, vol. 28, no. 12, pp. 1832–1843, Jun. 2010.
- [50] T.-J. Ahn, Y. Park, and J. Azaña, "Fast and accurate group delay ripple measurement technique for ultra-long chirped fiber Bragg gratings," *Opt. Lett.*, vol. 32, pp. 2674–2676, 2007.
- [51] T.-J. Ahn, Y. Park, D. J. Moss, S. Ramachandran, and J. Azaña, "Frequency-domain modal delay measurement for higher-order mode fiber based on stretched pulse interference," *Opt. Lett.*, vol. 33, pp. 19–21, 2008.
- [52] Y. Park, T.-J. Ahn, and J. Azaña, "Direct time-domain response of high-speed optical modulators based on stretched pulse interferometry," *Opt. Lett.*, vol. 32, pp. 3411–3413, 2007.
- [53] Y. Park, T.-J. Ahn, and J. Azaña, "Real-time complex temporal response measurements of ultrahigh-speed optical modulators," *Opt. Exp.*, vol. 17, pp. 1734–1745, 2009.
- [54] T. J. Ahn, Y. Park, and J. Azaña, "Real-time optical coherence tomography based on linearly-stretched pulse interference," in *Proc. CLEO/QELS*, 2008, Paper CFM4, pp. 1–2.
- [55] Y. Park, T.-J. Ahn, and J. Azaña, "Remote sensing in optical coherence tomography," presented at CLEO. San Jose, CA, 2008, Paper JTuA61.
- [56] S. Moon and D. Y. Kim, "Normalization detection scheme for high-speed optical frequency-domain imaging and reflectometry," *Opt. Exp.*, vol. 15, pp. 15129–15146, 2007.
- [57] A. Dawson. (2005, Sept.). Choosing a waveform instrument: DSO or digitizer? *Electronic Products Mag.* [Online] Available at: http://www.gage-applied.com/Applications/articles/DSO_or_Digitizer.pdf
- [58] R. Kashyap, *Fiber Bragg Gratings*, 2nd ed. London, U.K: Elsevier, 2010.
- [59] <http://www.proximion.com/products/DCM-CB,2011>
- [60] G. P. Agrawal, *Fiber-Optic Communication Systems*, 3rd ed. New-York: Wiley, 2002.
- [61] A. M. Weiner, *Ultrafast Optics*. Hoboken, NJ: Wiley, 2009.
- [62] L. R. Kawase, M. C. R. Carvalho, W. Margulis, and R. Kashyap, "Transmission of chirped optical pulses in fibre grating dispersion-compensated system," *Electron. Lett.*, vol. 33, pp. 152–154, 1997.
- [63] J. C. Cartledge, "Effect of modulator chirp and sinusoidal group delay ripple on the performance of systems using dispersion-compensating gratings," *J. Lightw. Technol.*, vol. 20, pp. 1918–1923, 2002.
- [64] T.-J. Ahn, Y. Park, and J. Azaña, "Real-time group delay ripple (GDR) measurement for chirped fiber Bragg gratings," in *Proc. OFC/NFOEC 2008*. San Diego, CA, OSA Tech. Dig. (CD), Paper JWA30.
- [65] C. D. Poole, J. M. Weisenfeld, D. J. DiGiovanni, and A. M. Vengsarkar, "Optical fiber-based dispersion-compensation using higher order modes near cutoff," *J. Lightw. Technol.*, vol. 12, pp. 1746–1758, 1994.

- [66] S. Ramachandran, "Dispersion-tailored few-mode fibers: A versatile platform for in-fiber photonic devices," *J. Lightw. Technol.*, vol. 23, pp. 3426–3443, 2005.
- [67] Q. Li, A. A. Au, C.-H. Lin, E. R. Lyons, and H. P. Lee, "An efficient all-fiber variable optical attenuator via acoustooptic mode coupling," *IEEE Photon. Technol. Lett.*, vol. 14, no. 11, pp. 1563–1565, Nov. 2002.
- [68] *Differential Mode Delay Measurement of Multimode Fiber in the Time Domain, Standards Document TIA-455-200-A*, 2003.
- [69] T.-J. Ahn and D. Y. Kim, "High-resolution differential mode delay measurement for a multimode optical fiber using a modified optical frequency domain reflectometer," *Opt. Exp.*, vol. 13, pp. 8256–8262, 2005.
- [70] J. Y. Lee, T.-J. Ahn, S. Moon, Y. C. Youk, Y. M. Jung, K. Oh, and D. Y. Kim, "Fourier-domain low-coherence interferometry for differential mode delay analysis of an optical fiber," *Opt. Lett.*, vol. 31, pp. 2396–2398, 2006.
- [71] T.-J. Ahn, S. Moon, S. Kim, K. Oh, D. Y. Kim, K. Schuster, and J. Kirchof, "Frequency-domain intermodal interferometer for the bandwidth measurement of a multimode fiber," *Appl. Opt.*, vol. 45, pp. 8238–8243, 2006.
- [72] F. P. Romstad, D. Birkedal, J. Mork, and J. A. Hvam, "Heterodyne technique for measuring the amplitude and phase transfer functions of an optical modulator," *IEEE Photon. Technol. Lett.*, vol. 14, no. 5, pp. 621–623, May 2002.
- [73] C. Dorrer, "Interferometric techniques for the characterization of temporal modulators," *IEEE Photon. Technol. Lett.*, vol. 17, no. 12, pp. 2688–2690, Dec. 2005.
- [74] C. Dorrer and I. Kang, "Simultaneous temporal characterization of telecommunication optical pulses and modulators by use of spectrograms," *Opt. Lett.*, vol. 27, pp. 1315–1317, 2002.
- [75] J. Azaña, "Design specifications of a time-domain spectral shaping optical system based on dispersion and temporal modulation," *Electron. Lett.*, vol. 39, pp. 1530–1532, 2003.
- [76] E. C. W. Lee, J. F. deBoer, M. Mujat, H. Lim, and S. H. Yun, "In vivo optical frequency domain imaging of human retina and choroid," *Opt. Exp.*, vol. 14, pp. 4403–4411, 2006.
- [77] C. Dorrer, "Temporal van Cittert-Zernike theorem and its application to the measurement of chromatic dispersion," *J. Opt. Soc. Am. B*, vol. 21, pp. 1417–1423, 2004.
- [78] Y. Park, A. Malacarne, and J. Azaña, "Real-time ultrawide-band group delay profile monitoring through quasi-incoherent processing," *Opt. Express*, vol. 19, pp. 3937–3944, 2011.
- [79] R. N. Bracewell, *The Fourier Transform and Its Applications*. New York: McGraw-Hill, ch. 12, 1965.



Tae-Jung Ahn was born in Sangju, Korea, on February 7, 1976. He received the M.S. and Ph.D. degrees in fiber optic engineering (photonic technologies) from Gwangju Institute of Science and Technology (GIST), Gwangju, Korea, in August 2000 and August 2006, respectively.

From September 2006 to early 2008, he was a Postdoctoral Research Fellow at the Centre Énergie Matériaux et Télécommunications, Institut National de la Recherche Scientifique (INRS), Montreal/Varenes, QC, Canada. During his graduate

courses and Postdoctoral position, he was granted a scholarship fully supported by Korea Science and Engineering Foundation (KOSEF), Korean Government. Since 2008, he has been with the Department of Photonic Engineering, Chosun University, Gwangju, Korea, as an Assistant Professor. He has authored or coauthored more than 60 international papers and conference contributions, in the fields of optical frequency-domain reflectometry, optical device characterization, pulse characterization, optical-fiber technology, optical-fiber sensors, fiber gratings, and optical communications. He has taught courses on optoelectronics and photonics, optical communications, Fourier optics, and optical metrology. His current research interests include fiber gratings, fiber sensors, optical interferometry, and ultrafast optical-signal processing. In particular, his expertise ranges from the fabrication of specialty optical fibers to ultrafast measurement system based on fiber optics.

Prof. Ahn is a member of the Optical Society of America. He received the Best Research Award from GIST and the Gold Prize in 12th SAMSUNG HumanTech Thesis Prize (2006).



Yongwoo Park received the Ph.D. degree in information and communication engineering from Gwangju Institute of Science and Technology (GIST), Gwangju, Korea, in 2002.

He was with the Basic Research Laboratory, Electronics and Telecommunications Research Institute (ETRI), Korea, until 2005. He was a Postdoctoral Research Fellow at the Institut National de la Recherche Scientifique (INRS), Centre Énergie Matériaux et Télécommunications, Montreal/Varenes, QC, Canada, until 2008, where

he is currently a Research Associate. His current research interests include a wide range of topics, including fiber optics, ultrafast photonic signal processing, optical-signal characterization, real-time photonic device characterization, optical telecommunications, all-optical computing, optical metrology, and biomedical imaging. He has authored or coauthored more than 140 publications in top scientific journals and leading technical conferences, including more than 62 publications in the Science Citation Index (SCI) journals. He holds more than 38 patents including 13 U.S. patents.



José Azaña (M'01) was born in Toledo, Spain. He received the Telecommunication Engineer degree (six years engineering program) and the Ph.D. degree in telecommunication engineering from the Universidad Politécnica de Madrid (UPM), Madrid, Spain, in 1997 and 2001, respectively. He completed a part of his Ph.D. research from the University of Toronto, Toronto, ON, Canada (1999) and a part from the University of California, Davis, (2000).

From September 2001 to mid-2003, he was a Postdoctoral Research Fellow at McGill University Montreal, Montreal, QC, Canada. In 2003, he was appointed as an Assistant Professor at the Institut National de la Recherche Scientifique, Centre Énergie, Matériaux et Télécommunications (INRS-EMT), Montreal. He was promoted to Associate Professor in 2006 and to Full Professor in 2010. His current research interests cover a wide range of topics, including all-fiber grating technologies, ultrafast photonic signal processing, optical pulse shaping, fiber-optic telecommunications, all-optical computing, measurement of ultrafast events, light-pulse interferometry, and microwave-waveform generation and manipulation. He has authored or coauthored nearly 125 publications in top scientific journals and leading technical conferences, including more than 120 publications in high-impact peer-reviewed journals and various invited and coinvented presentations in international meetings.

Prof. Azaña is a member of the Optical Society of America. He was a Guest Editor of two monographs devoted to the area of Optical Signal Processing, published by the European Association for Signal Processing (EURASIP) *J. Appl. Signal Proc.* (2005) and *Journal of Lightwave Technology* (2006). He has been recognized with several awards and distinctions, including the XXII National Prize for the "Best Doctoral Thesis in Data Networks" from the Association of Telecommunication Engineers of Spain (2002), the "Extraordinary Prize for the Best Doctoral Thesis" from his former university, Universidad Politécnica de Madrid (UPM) (2003), the 2008 IEEE Photonics Society (formerly LEOS) Young Investigator Award, and the 2009 IEEE-Microwave Theory and Technique (MTT) Society Microwave Prize.